Comparison of the lattice Boltzmann and pseudo-spectral methods for decaying turbulence: Low-order statistics

Yan Peng [a], Wei Liao [a], Li-Shi Luo [a,*], Lian-Ping Wang [b]

[a] *Department of Mathematics & Statistics, Center for Computational Sciences, Old Dominion University, Norfolk, VA 23529, USA*
[b] *Department of Mechanical Engineering, University of Delaware, 126 Spencer Laboratory, Newark, DE 19716-3140, USA*

ARTICLE INFO

ABSTRACT

We conduct a detailed comparison of the lattice Boltzmann equation (LBE) and the pseudo-spectral (PS) methods for direct numerical simulations (DNS) of the decaying homogeneous isotropic turbulence in a three-dimensional periodic cube. We use a mesh size of $N^3 = 128^3$ and the Taylor micro-scale Reynolds number $24.35 \leqslant \mathrm{Re}_\lambda \leqslant 72.37$, and carry out all simulations to $t \approx 30\tau_0$, where τ_0 is the turbulence turn-over time. In the PS method, the second-order Adam–Bashforth scheme is used to numerically integrate the nonlinear term while the viscous term is treated exactly. We compare the following quantities computed by the LBE and PS methods: instantaneous velocity $\boldsymbol{u}$ and vorticity ω fields, and statistical quantities such as, the total energy $K(t)$ and the energy spectrum $E(k,t)$, the dissipation rate $\varepsilon(t)$, the root-mean-squared (rms) pressure fluctuation $\delta p(t)$ and the pressure spectrum $P(k,t)$, and the skewness and flatness of the velocity derivative. Our results show that the LBE method performs very well when compared to the PS method in terms of accuracy and efficiency: the instantaneous flow fields, $\boldsymbol{u}$ and ω, and all the statistical quantities — except the rms pressure fluctuation $\delta p(t)$ and the pressure spectrum $P(k,t)$ — computed from the LBE and PS methods agree well with each other, provided that the initial flow field is adequately resolved by both methods. We note that $\delta p(t)$ and $P(k,t)$ computed from the two methods agree with each other in a period of time much shorter than that for other quantities, indicating that the pressure field p computed by using the LBE method is less accurate than other quantities. The skewness and flatness computed from the LBE method contain high-frequency oscillations due to acoustic waves in the system, which are absent in PS methods. Our results indicate that the resolution requirement for the LBE method is $\delta x/\eta_0 \leqslant 1.0$, approximately twice of the requirement for PS methods, where δx and η_0 are the grid spacing and the initial Kolmogorov length, respectively. Overall, the LBE method is shown to be a reliable and accurate method for the DNS of decaying turbulence.

1. Introduction

Homogeneous isotropic turbulence in three-dimensions (3D) is a canonical case in turbulence theory (cf. [1,2] and references therein). To date, pseudo-spectral (PS) methods [3,4] remain as the most accurate numerical tool for direct numerical simulations (DNS) of homogeneous isotropic turbulence (HIT) (*e.g.*, [5–15]). While PS methods are the preferred method for DNS of flows with simple geometries, such as the channel flow with flat walls or turbulence in a cube with periodic boundary conditions, PS methods may be difficult to apply for flows with complex geometries of engineering significance. Development of accurate and efficient methods for DNS of turbulent flows is one of the most active areas in computational fluid dynamics. In this work, we will use the lattice Boltzmann method (*e.g.*, [16–18]) for DNS of decaying homogeneous isotropic turbulence (DHIT) in three-dimensions (3D).

The purpose of the present work is to validate the lattice Boltzmann method for DNS of decaying turbulence in three dimensions. The focus of this work is on the accuracy and efficiency of the interested numerical methodology, but not on the physics of turbulence. The validation will be carried out by conducting a detailed comparison of the lattice Boltzmann and the pseudo-spectral methods in terms of accuracy and efficiency for decaying turbulence in 3D. The lattice Boltzmann method has been applied for DNS of homogeneous turbulence [19–29]. In particular, there has been previous studies using the LBE method for DNS of decaying turbulence [19–24]. However, the previous studies [19–24] offer only *qualitative* comparisons for a very limited number of low-order statistical quantities such as the total kinetic energy $K(t)$, the dissipation rate $\varepsilon(t)$, and the energy spectrum $E(\boldsymbol{k}, t)$ in a relatively short period of time. We note that there are some comparative studies of finite-difference and spectral methods [30,31], which are restricted low-order turbulence statistics.

* Corresponding author. Tel.: +1 757 683 5295; fax: +1 757 683 3885.
E-mail addresses: ypeng@odu.edu (Y. Peng), wliao@odu.edu (W. Liao), lluo@odu.edu (L.-S. Luo), lwang@udel.edu (L.-P. Wang).
URL: http://www.lions.odu.edu/lluo (L.-S. Luo).

In this work we will compare in detail the lattice Boltzmann and pseudo-spectral methods for decaying turbulence in 3D by computing a number of low-order statistical quantities, in addition to $K(t)$, $\varepsilon(t)$, and $E(\mathbf{k}, t)$, such as the skewness and the flatness, and the pressure spectrum $P(\mathbf{k}, t)$. In addition, we will compare the instantaneous velocity and vorticity fields obtained by the two methods. The simulations will be carried out for about $30\tau_0$, where τ_0 is the turbulence turnover time. The direct comparison will allow us to investigate, first, the differences between the two methods and, second, the effects of the differences on the quantities relevant to decaying turbulence.

The remainder of this paper is organized as follows. Section 2 succinctly describes the lattice Boltzmann and pseudo-spectral methods. Section 3 gives a brief discussion of the decaying turbulence, its initial conditions, and the quantities to be computed. Section 4 presents our results as the following. Section 4.1 describes the parameters and conditions used in our simulations. Section 4.2 compares the instantaneous velocity and vorticity fields obtained by using the LBE and PS methods with a grid size $N^3 = 128^3$ and the Taylor micro-scale Reynolds number $\mathrm{Re}_\lambda \approx 24.35$. Section 4.3 presents the statistical quantities computed by using the two methods. Section 4.4 analyzes the acoustic waves in the LBE simulations, which are absent in the PS simulations. Section 4.5 investigates the dependence of instantaneous flow fields and statistical quantities on the viscosity v or the Reynolds number Re_λ. Various results with $24.35 \leqslant \mathrm{Re}_\lambda \leqslant 72.37$ will be discussed. Section 4.6 compares the computational efficiency of the two methods. Finally, Section 5 summarizes our results and concludes the paper.

2. Numerical methods

2.1. The lattice Boltzmann equation

We use the lattice Boltzmann equation with the multiple-relaxation-time (MRT) collision model [32–36] and 19 discrete velocities in three dimensions, i.e., the D3Q19 model [35]. The MRT-LBE can be concisely written as the following:

$$\mathbf{f}(\mathbf{x}_j + \mathbf{c}\delta t, t_n + \delta t) = \mathbf{f}(\mathbf{x}_j, t_n) - \mathsf{M}^{-1} \cdot \mathsf{S} \cdot [\mathbf{m} - \mathbf{m}^{(eq)}], \tag{1}$$

where the symbols in bold-font are Q-tuple vectors in $\mathbb{R}^Q$ for a model with Q discrete velocities,

$$\mathbf{f}(\mathbf{x}_j, t_n) := (f_0(\mathbf{x}_j, t_n), f_1(\mathbf{x}_j, t_n), \ldots, f_b(\mathbf{x}_j, t_n))^\dagger,$$
$$\mathbf{f}(\mathbf{x}_j + \mathbf{c}\delta t, t_n + \delta t) := (f_0(\mathbf{x}_j, t_n + \delta t), f_1(\mathbf{x}_j + \mathbf{c}_1\delta t, t_n + \delta t),$$
$$\ldots, f_b(\mathbf{x}_j + \mathbf{c}_b\delta t, t_n + \delta t))^\dagger,$$
$$\mathbf{m}(\mathbf{x}_j, t_n) := (m_0(\mathbf{x}_j, t_n), m_1(\mathbf{x}_j, t_n), \ldots, m_b(\mathbf{x}_j, t_n))^\dagger,$$
$$\mathbf{m}^{(eq)}(\mathbf{x}_j, t_n) := (m_0^{(eq)}(\mathbf{x}_j, t_n), m_1^{(eq)}(\mathbf{x}_j, t_n), \ldots, m_b^{(eq)}(\mathbf{x}_j, t_n))^\dagger,$$

$\dagger$ denotes transpose, f_i is the discrete particle density distribution function corresponding to the discrete velocity $\mathbf{c}_i, i \in \{0, 1, \ldots, b\}$, and m_i is the ith moment. The $Q \times Q$ matrix M transforms $\mathbf{f}$ to $\mathbf{m}$:

$$\mathbf{m} = \mathsf{M} \cdot \mathbf{f}, \quad \mathbf{f} = \mathsf{M}^{-1} \cdot \mathbf{m}. \tag{2}$$

By construction the transform matrix M has the property that $\mathsf{M} \cdot \mathsf{M}^\dagger$ is diagonal, thus M^{-1} can be easily obtained [33,35,36].

For the D3Q19 model [35], the 19 discrete velocities are

$$\mathbf{c}_i = \begin{cases} (0, 0, 0), & i = 0, \\ (\pm 1, 0, 0)c, \ (0, \pm 1, 0)c, \ (0, 0, \pm 1)c, & i = 1\text{--}6, \\ (\pm 1, \pm 1, 0)c, \ (\pm 1, 0, \pm 1)c, \ (0, \pm 1, \pm 1)c, & i = 7\text{--}18, \end{cases} \tag{3}$$

where $c := \delta x / \delta t$. The corresponding 19 moments are

$$\mathbf{m} := (\delta\rho, e, \epsilon, j_x, q_x, j_y, q_y, j_z, q_z, 3p_{xx}, 3\pi_{xx}, p_{ww}, \pi_{ww},$$
$$p_{xy}, p_{yz}, p_{xz}, m_x, m_y, m_z)^\dagger = (m_0, m_1, \ldots, m_{18})^\dagger, \tag{4}$$

where $\delta\rho$ is the density fluctuation, the density

$$\rho := \rho_0 + \delta\rho, \quad \rho_0 = 1, \tag{5}$$

and ρ_0 is the mean density. The effect due to round-off error can be reduced by using $\delta\rho$ instead of ρ in the LBE simulations [37]. The equilibria of the moments are functions of the conserved quantities in the system, i.e., the density fluctuation $\delta\rho$ and the flow momentum $\mathbf{j} = (j_x, j_y, j_z) := \rho_0 \mathbf{u}$ [35]:

$$\delta\rho = \sum_{i=0}^{Q-1} f_i, \quad \mathbf{j} := \rho_0 \mathbf{u} = \sum_{i=0}^{Q-1} f_i \mathbf{c}_i, \tag{6}$$

where we have applied the approximation for incompressible flows, i.e.,

$$\mathbf{j} = \rho \mathbf{u} \approx \rho_0 \mathbf{u} = \mathbf{u}. \tag{7}$$

That is, we assume that in theory $|\delta\rho| \ll 1$, therefore we can neglect the coupling terms between $\delta\rho$ and $\mathbf{u}$. The equilibria of the non-conserved moments in the D3Q19 model for athermal flows are [35]:

$$e^{(eq)} = -11\delta\rho + \frac{19}{\rho_0}\mathbf{j} \cdot \mathbf{j}, \tag{8a}$$

$$\epsilon^{(eq)} = 3\delta\rho - \frac{11}{2\rho_0}\mathbf{j} \cdot \mathbf{j}, \tag{8b}$$

$$q_x^{(eq)} = -\frac{2}{3}j_x, \quad q_y^{(eq)} = -\frac{2}{3}j_y, \quad q_z^{(eq)} = -\frac{2}{3}j_z, \tag{8c}$$

$$p_{xx}^{(eq)} = \frac{1}{3\rho_0}\left[2j_x^2 - \left(j_y^2 + j_z^2\right)\right], \quad p_{ww}^{(eq)} = \frac{1}{\rho_0}\left[j_y^2 - j_z^2\right], \tag{8d}$$

$$p_{xy}^{(eq)} = \frac{1}{\rho_0}j_x j_y, \quad p_{yz}^{(eq)} = \frac{1}{\rho_0}j_y j_z, \quad p_{xz}^{(eq)} = \frac{1}{\rho_0}j_x j_z, \tag{8e}$$

$$\pi_{xx}^{(eq)} = -\frac{1}{2}p_{xx}^{(eq)}, \quad \pi_{ww}^{(eq)} = -\frac{1}{2}p_{ww}^{(eq)}, \tag{8f}$$

$$m_x^{(eq)} = m_y^{(eq)} = m_z^{(eq)} = 0, \tag{8g}$$

where $\mathbf{j} \cdot \mathbf{j} := j_x^2 + j_y^2 + j_z^2 = u_x^2 + u_y^2 + u_z^2$. The significance of the moments has been discussed previously [33,35,36].

The diagonal relaxation matrix S is positive and its diagonal elements are relaxation rates, which must satisfy the stability condition $s_i > 1/2$ for all non-conserved moments [33,35,36],

$$\mathsf{S} = \mathrm{diag}(0, s_1, s_2, 0, s_4, 0, s_4, 0, s_4, s_9, s_{10}, s_9, s_{10}, s_{13}, s_{13}, s_{13}, s_{16}, s_{16}, s_{16})$$
$$= \mathrm{diag}(0, s_e, s_\epsilon, 0, s_q, 0, s_q, 0, s_q, s_v, s_\pi, s_v, s_\pi, s_v, s_v, s_v, s_m, s_m, s_m). \tag{9}$$

The speed of sound of the D3Q19 model is $c_s = \left(1/\sqrt{3}\right)c$ and the shear viscosity v and the bulk viscosity ζ are

$$v = \frac{1}{3}\left(\frac{1}{s_v} - \frac{1}{2}\right)c\,\delta x, \tag{10a}$$

$$\zeta = \frac{(5 - 9c_s^3)}{9}\left(\frac{1}{s_e} - \frac{1}{2}\right)c\,\delta x. \tag{10b}$$

With the equilibria of Eqs. (8g), if all of the relaxation rates, $\{s_i | i = 0, \ldots, 18\}$, are set to be a single value $1/\tau$, i.e., $\mathsf{S} = \tau^{-1}\mathsf{I}$, where I is $Q \times Q$ identity matrix, then the model is equivalent to the D3Q19 LBGK model of which the equilibria are the second-order Taylor expansion of the Maxwellian distribution function in $\mathbf{u}$. Except s_v, which is determined by the viscosity v, other relaxation rates s_i may be determined by linear stability analysis [33,35,36]. The specific values of s_i used in our simulations will be given explicitly in Section 4.1.

The LBE algorithm consists of two steps: collision and advection. For a given LBE model, the collision is the only step involving arithmetic operations, and the number of arithmetic operations at each grid node is fixed, while the advection moves data from one grid node to another with no arithmetic operation. However, advection does cost CPU time for passing data. Thus, the best way to implement LBE code is to combine the collision and advection in one step so that data passing time overlaps with the CPU time for floating point operations. In the present work, we still implement collision and advection into two do loops so that the code is easier to modularize and maintain. Obviously, for a system of size N^3, the overall computational cost of the LBE method is of $O(N^3)$ per time step.

2.2. The pseudo-spectral method

The pseudo-spectral (PS) method solves the incompressible Navier–Stokes equations in a cubic domain of size L^3 with periodic boundary conditions:

$$\partial_t \boldsymbol{u} + \boldsymbol{u} \cdot \nabla \boldsymbol{u} = -\nabla p + \nu \nabla^2 \boldsymbol{u}, \quad \boldsymbol{x} \in [0, L]^3, \tag{11a}$$

$$\nabla \cdot \boldsymbol{u} = 0, \tag{11b}$$

where the velocity field $\boldsymbol{u}(\boldsymbol{x}, t)$ is represented as a finite Fourier series

$$\boldsymbol{u}(\boldsymbol{x}, t) = \sum_{\boldsymbol{k}} \tilde{\boldsymbol{u}}(\boldsymbol{k}, t) e^{\iota \boldsymbol{k} \cdot \boldsymbol{x}}, \tag{12}$$

where $\iota := \sqrt{-1}$. Usually, $L = 2\pi$, the grid resolution N in each dimension is an even number, and the grid spacing is $\delta x = 2\pi/N$. The wavenumber $k_i, i \in \{x, y, z\}$, in each dimension varies between $-N/2 + 1$ and $N/2$ and the largest wavenumber is $k_N = N/2$. The fast Fourier transform (FFT) is used to compute $\tilde{\boldsymbol{u}}$. We use the open source package FFTW 2.1.5 (cf. http://www.fftw.org) for FFT with MPI (cf. http://www-unix.mcs.anl.gov/mpi and http://computing.llnl.gov/tutorials/mpi) in our simulations.

For pseudo-spectral methods, in order to reduce computational cost, the nonlinear advection term $\boldsymbol{u} \cdot \nabla \boldsymbol{u}$ term is evaluated in physical space as the following. Both the velocity $\tilde{\boldsymbol{u}}$ and the vorticity $\tilde{\omega}$ in Fourier space are transformed by the inverse FFT back to physical space to form the nonlinear term $\omega \times \boldsymbol{u}$, which is then transformed back to wavenumber space $\boldsymbol{k}$. The de-aliasing is accomplished by nullifying $\tilde{\boldsymbol{u}}(\boldsymbol{k}, t)$ for $|\boldsymbol{k}| > N/3$ at each time step.

The incompressible Navier–Stokes equation can be re-written in $\boldsymbol{k}$ space as the following:

$$\partial_t \tilde{\boldsymbol{u}} + \nu k^2 \tilde{\boldsymbol{u}} = -\tilde{\boldsymbol{T}}_\perp, \tag{13}$$

where $\tilde{\boldsymbol{T}}$ is the Fourier transform of $\omega \times \boldsymbol{u}$,

$$\tilde{\boldsymbol{T}}_\perp := \tilde{\boldsymbol{T}} - (\tilde{\boldsymbol{T}} \cdot \hat{\boldsymbol{k}}) \hat{\boldsymbol{k}},$$

and $\hat{\boldsymbol{k}}$ is the unit vector parallel to $\boldsymbol{k}$. Eq. (13) can be further written as

$$\partial_t (\tilde{\boldsymbol{u}} e^{\nu k^2 t}) = -\tilde{\boldsymbol{T}}_\perp e^{\nu k^2 t}. \tag{14}$$

We will apply the second-order Adams–Bashforth scheme for time integration of the above equation:

$$\tilde{\boldsymbol{u}}(t + \delta t) = \left\{ \tilde{\boldsymbol{u}}(t) - \frac{1}{2} \delta t \left[3 \tilde{\boldsymbol{T}}_\perp(t) - \tilde{\boldsymbol{T}}_\perp(t - \delta t) e^{-\nu k^2 \delta t} \right] \right\} e^{-\nu k^2 \delta t}. \tag{15}$$

Eq. (13) circumvents the need to directly solve the Poisson equation for the pressure p by noting the fact that

$$\tilde{p} = \iota \frac{\tilde{T}_\parallel}{k} - \tilde{\kappa}, \qquad \tilde{T}_\parallel := \hat{\boldsymbol{k}} \cdot \tilde{\boldsymbol{T}}, \tag{16}$$

where $\tilde{\kappa}$ is the Fourier transform of the kinetic energy $\boldsymbol{u} \cdot \boldsymbol{u}/2$. Therefore, the pressure p is obtained by computing the inverse Fourier transform of $\tilde{p}$ given by the above equation.

For homogeneous turbulence with a mesh of size N^3, the computational cost of the pseudo-spectral method is of the order $O(N^3 \ln N)$ per time step, while that of the LBE method is of $O(N^3)$. For homogeneous turbulence, pseudo-spectral methods are the chosen method for their superiority in spatial accuracy.

3. Decaying homogeneous isotropic turbulence in a 3D cube

The decaying homogeneous isotropic turbulence (DHIT) in a three-dimensional cube of the size $L^3 = (2\pi)^3$ with periodic boundary conditions in all three directions is a canonical problem in turbulence theory. It has been used as a standard test case to validate numerical schemes for direct numerical simulations. In the DHIT, an initial energy spectrum is given in Fourier space $\boldsymbol{k}$. In the present work, the following initial spectrum is used:

$$E_0(k) := E(k, t = 0) = A k^4 e^{-0.14 k^2}, \qquad k \in [k_a, k_b], \tag{17}$$

where the magnitude A and the range of the initial energy spectrum $[k_a, k_b]$ determine the initial total kinetic energy K_0 in the simulation. The divergence-free initial velocity field $\boldsymbol{u}_0$, i.e., $\nabla \cdot \boldsymbol{u}_0 = 0$, is generated in Fourier space $\boldsymbol{k}$ according to Rogallo's procedure [38]:

$$\tilde{\boldsymbol{u}}_0(\boldsymbol{k}) = \left(\frac{\alpha k k_2 + \beta k_1 k_3}{k \sqrt{(k_1^2 + k_2^2)}} \right) \hat{\boldsymbol{k}}_1 + \left(\frac{\beta k_2 k_3 - \alpha k_1 k}{k \sqrt{(k_1^2 + k_2^2)}} \right) \hat{\boldsymbol{k}}_2 - \left(\frac{\beta \sqrt{(k_1^2 + k_2^2)}}{k} \right) \hat{\boldsymbol{k}}_3, \tag{18}$$

where $\alpha = \sqrt{E_0(k)/4\pi k^2} \, e^{\iota \theta_1} \cos \phi, \beta = \sqrt{E_0(k)/4\pi k^2} \, e^{\iota \theta_2} \sin \phi; \theta_1, \theta_2$ and ϕ are uniform random variables between 0 and $2\pi; \iota := \sqrt{-1}$; and $\hat{\boldsymbol{k}}_1, \hat{\boldsymbol{k}}_2,$ and $\hat{\boldsymbol{k}}_3$ are the unit vectors along three axis in $\boldsymbol{k}$-space. The turbulent fluctuating velocity field $\boldsymbol{u}$ has a zero mean, i.e., $\langle \boldsymbol{u} \rangle = 0$, and is characterized by its root-mean-squared (rms) value:

$$u' := \frac{1}{\sqrt{3}} \sqrt{\langle \boldsymbol{u} \cdot \boldsymbol{u} \rangle}, \tag{19}$$

where $\langle \cdot \rangle$ designates ensemble average, which can be carried out as volume average in either physical space $\boldsymbol{x}$ or spectral space $\boldsymbol{k}$.

We will compare instantaneous velocity field $\boldsymbol{u}(\boldsymbol{x}_j, t_n)$ and vorticity field $\omega(\boldsymbol{x}_j, t_n)$ obtained from the LBE and PS methods. The vorticity fields $\omega(\boldsymbol{x}_j, t_n)$ in both methods will be computed in spectral space $\boldsymbol{k}$ by the inverse FFT of $\tilde{\omega} = -\iota \boldsymbol{k} \times \tilde{\boldsymbol{u}}$. We compute the energy spectrum $E(\boldsymbol{k}, t)$ and the compensated spectrum $\Psi(k)$ of the velocity field $\boldsymbol{u}(\boldsymbol{x}, t)$,

$$E(\boldsymbol{k}, t) := \frac{1}{2} \tilde{\boldsymbol{u}}(\boldsymbol{k}, t) \cdot \tilde{\boldsymbol{u}}^\dagger(\boldsymbol{k}, t), \tag{20a}$$

$$\Psi(k) := \varepsilon(k)^{-2/3} k^{5/3} E(k), \tag{20b}$$

and other statistical quantities pertinent to DHIT:

$$K(t) := \frac{1}{2} \langle \boldsymbol{u} \cdot \boldsymbol{u} \rangle = \int d\boldsymbol{k} \, E(\boldsymbol{k}, t), \tag{21a}$$

$$\Omega(t) := \langle (\nabla \boldsymbol{u})^2 \rangle = \int d\boldsymbol{k} \, k^2 E(\boldsymbol{k}, t), \tag{21b}$$

$$\varepsilon(t) := 2\nu \Omega(t), \quad \eta := \sqrt[4]{\nu^3/\varepsilon}, \tag{21c}$$

$$S_{u_i}(t) = \frac{\langle (\partial_i u_i)^3 \rangle}{\langle (\partial_i u_i)^2 \rangle^{3/2}}, \qquad S_u(t) = \frac{1}{3} \sum_i S_{u_i}, \tag{21d}$$

$$F_{u_i}(t) = \frac{\langle (\partial_i u_i)^4 \rangle}{\langle (\partial_i u_i)^2 \rangle^2}, \qquad F_u(t) = \frac{1}{3} \sum_i F_{u_i}, \tag{21e}$$

where $K(t), \Omega(t),$ and $\varepsilon(t)$ are the total kinetic energy, the enstrophy, and the dissipation rate, respectively; η is the Kolmogorov length scale; $S_{u_i}(t)$ is the skewness computed from $\partial_i u_i, i \in \{x, y, z\}$, and $S_u(t)$ is the skewness averaged over three directions; and $F_{u_i}(t)$ is

the flatness computed from u_i and $F_u(t)$ is the flatness averaged over three directions. We also compute the pressure spectrum $P(k)$,

$$\langle (\delta p)^2 \rangle = \int d\mathbf{k} P(k), \qquad (22)$$

where δp is the pressure fluctuation. For the DHIT, the Taylor micro-scale Reynolds number Re_λ is used to characterize the flow:

$$Re_\lambda := \frac{u'\lambda}{v}, \quad \lambda := \sqrt{\frac{15}{2\Omega}} u', \qquad (23)$$

where λ is the transverse Taylor micro-scale length.

Because the LBE method is intrinsically a compressible flow solver, we monitor the rms velocity divergence

$$\Theta'(t) := \sqrt{\langle (\nabla \cdot \mathbf{u})^2 \rangle}. \qquad (24)$$

Note that for incompressible flows, $\nabla \cdot \mathbf{u} = 0$, thus $\Theta' = 0$ and $\Omega = \langle \boldsymbol{\omega} \cdot \boldsymbol{\omega} \rangle / 2$, where $\boldsymbol{\omega} := \nabla \times \mathbf{u}$ is the vorticity. We also monitor the Mach number in the LBE simulations,

$$Ma = \frac{u}{c_s}, \quad c_s = \sqrt{RT}, \qquad (25)$$

where $RT = \frac{1}{3}c^2$ and $c := \delta x / \delta t$.

4. Results

4.1. Parameters and flow conditions

To compare two significantly different methods such as the LBE and PS methods, we must first properly choose a number of parameters used in the simulation so that the comparison is meaningful. First of all, the simulations carried out to compare the two methods should have the same system size $L^3 = (2\pi)^3$ and the grid resolution N^3, the initial Taylor micro-scale Reynolds number Re_λ, and the dimensionless time step size dt' normalized by the turbulence turnover time $\tau_0 = K_0/\varepsilon_0$. The grid spacing is $\delta x = 2\pi/N$. In the LBE method, all quantities are in the units of $\delta x = \delta t = 2\pi/N$. In the PS method, $\delta x = 2\pi/N$, the initial kinetic energy K_0 is always set to 1, therefore the initial rms velocity is $u_0' = \sqrt{2/3}$. With equal initial Re_λ and the *dimensionless* time step size dt', both the viscosity v and the time step size dt in the PS calculations must be related to their LBE counterpart as the following:

$$v_{PS} = \frac{v_{LBE}}{\sqrt{K_0}}, \quad \delta t_{PS} = \sqrt{K_0}\, \delta t_{LBE}, \qquad (26)$$

where K_0 is the initial total kinetic energy in the LBE simulation computed from Eq. (17) with given parameter values of A, k_a and k_b. Table 1 summarizes the relationships between various quantities in the LBE and PS methods.

For the initial energy spectrum $E_0(k)$ given by Eq. (17), we use $A = 1.4293 \times 10^{-4}$, $k_a = 3$, and $k_b = 8$, thus the initial kinetic energy is $K_0 \approx 1.0130 \times 10^{-2}$, the rms velocity is $u' \approx 8.2181 \times 10^{-2}$, and the initial enstrophy is $\Omega_0 \approx 0.2077$.

For the LBE method, we must ensure that the local Mach number Ma is small enough so that the LBE method is well within the incompressible flow region. With the initial energy spectrum and

parameters given above, we can ensure that the maximum local Mach number $Ma_{max} = \|\mathbf{u}_0\|_{max}/c_s \leqslant 0.15$ for the initial velocity field $\mathbf{u}_0$, where $c_s = \left(1/\sqrt{3}\right)c$ is the sound speed in the LBE model. The viscosity used in the LBE simulations is $v = (1/600)c\delta x$. With the initial energy spectrum $E_0(k)$ and the viscosity v given above, the Taylor micro-scale Reynolds $Re_\lambda \approx 24.35$.

In the LBE simulations, we set the values of the relaxation rates for all non-conserved moments, except the stresses, as $s_i = 1.8 \neq s_v$. We have also tested other values of $s_i \neq s_v$, and have found that, within a certain range, they have little noticeable effect on the results of DHIT.

For homogeneous isotropic turbulence with a given Re_λ, the required resolution for DNS in 3D using *spectral* methods can be estimated as (cf. [39,1]):

$$N \geqslant 0.4 Re_\lambda^{3/2}. \qquad (27)$$

The above formula can be re-written in terms of the Kolmogorov length scale η normalized by the grid spacing δx [1]:

$$\frac{\eta}{\delta x} \geqslant \frac{1}{2.1} \approx 0.476. \qquad (28)$$

Since the lattice Boltzmann method is formally a second-order method [40,41], the resolution requirement for the LBE method would not be the same as the above criterion (28) for spectral methods, which are *exponentially* accurate. Thus, for the LBE method we should consider a resolution criterion more stringent than Eq. (28), such as

$$\frac{\eta}{\delta x} \geqslant 1.0. \qquad (29)$$

The above criterion is consistent with previous empirical observations (cf. [42,43]) and will be tested in our simulations.

4.2. Instantaneous velocity and vorticity fields

First, we will directly compare instantaneous flow fields obtained with the LBE and PS methods with $Re_\lambda \approx 24.35$. The initial velocity fields used in both the LBE and PS methods are identical except an overall scaling factor, as discussed in the previous section. That is, one single random velocity field is generated with the energy spectrum of Eq. (17), then it is rescaled such that $u_0' = \sqrt{2/3}$ for the PS method, and $Ma_{max} \leqslant 0.15$ for the LBE method. For the PS method, the pressure p is obtained by solving the Poisson equation in the spectral space. As for the LBE method, p is obtained by using an iterative procedure which solves the Poisson equation consistent with the LBE method [44]. Before we compare the results obtained by the LBE and PS methods, we should bear in mind that these two methods are different from each other. Specifically, the PS method solves the incompressible Navier–Stokes equation with an *exponential* accuracy in space for all flow variables, while the LBE method is formally second-order accurate in space for the velocity field $\mathbf{u}$ and only first-order accurate for the pressure field p [40,41]. As for the accuracy in time, the PS method is second-order, while formally the LBE method is only first-order [41]. In some way the LBE method can be viewed as a Navier–Stokes solver with artificial compressibility.

We first show the evolution of the magnitude of the velocity field normalized by its initial rms value $\|\bar{\mathbf{u}}\| := \|\mathbf{u}/u_0'\|$ on. The system size is 128^3 and the Taylor micro-scale Reynolds number is $Re_\lambda \approx 24.35$ unless it is otherwise stated. We compare results from three runs with an identical initial velocity field apart from an overall constant factor: the LBE method, the PS method with the dimensionless time step size dt' equal to that of the LBE method (labeled as PS1), and the PS method with the dimensionless time step size equal to one third of that in the LBE method (labeled as PS2). The dimensionless time step size, normalized by the

Table 1
Parameters used in the lattice Boltzmann (LBE) and pseudo-spectral (PS) methods. K_0 and ε_0 are the initial total kinetic energy and dissipation rate in the LBE simulations, respectively, computed from the initial spectrum $E_0(k)$ given by Eq. (17) with parameters A, k_a, and k_b.

Method	K_0	u_0'	v	L	δx	δt	$\delta t'$
LBE	K_0	$\sqrt{2K_0/3}$	v	2π	$2\pi/N$	$2\pi/N$	$2\pi\varepsilon_0/K_0 N$
PS	1	$\sqrt{2/3}$	$v/\sqrt{K_0}$	2π	$2\pi/N$	$2\pi\sqrt{K_0}/N$	$2\pi\varepsilon_0/K_0 N$

turbulence turnover time $\tau_0 = K_0/\varepsilon_0$, is $\delta t' = 4\pi\nu\Omega_0/NK_0 \approx 2.892 \times 10^{-3}$. All runs stop at $t' \approx 30$, when the total kinetic energy K decays almost four orders of magnitude, and the rms velocity u' decays almost two orders of magnitude.

The results for the evolution of $\|\bar{\boldsymbol{u}}\|$ on the xy plane $z = \pi$ are shown in Fig. 1. We compare the results obtained by the three runs in four instances: $t' \approx 4.048, 8.095, 16.189$, and 29.949. Even at the latest time $t' \approx 29.949$, the velocity field $\bar{\boldsymbol{u}}$ obtained from the LBE method is very similar to those obtained from the PS method with an equal time step size $\delta t'$ or a smaller one (i.e., $\delta t'/3$): both magnitudes and locations of vortices in the velocity fields obtained by different methods are very close to each other.

The agreement between the flow fields is further demonstrated with the evolution of the vorticity field normalized by the initial rms velocity $\|\bar{\omega}\| := \|\omega\|L/u'_0$ on a plane. The vorticity fields for both LBE and PS simulations are computed in spectral space $\boldsymbol{k}$, $\tilde{\omega} = -\imath\boldsymbol{k} \times \tilde{\boldsymbol{u}}$, and then by using the inverse FFT to transfer $\tilde{\omega}$ back to physical space $\boldsymbol{x}$. The results of $\|\bar{\omega}\|$ are shown in Fig. 2. Clearly, at $t' \approx 29.949$, the difference between the LBE and PS vorticity fields is visible in Fig. 2. While the basic features of the vorticity fields obtained from the LBE and PS methods remain quite similar, in terms of vortex shapes and locations, the LBE and PS results clearly deviate from each other more and more as time evolves.

We also show the evolutions of velocity and vorticity magnitude iso-surfaces in three dimensions in Figs. 3 and 4, respectively. We show the iso-surfaces of velocity and vorticity magnitudes in three times: $t' = 0.1348, 0.2359$, and 0.5730, corresponding to the times before, about, and after the dissipation rate $\varepsilon(t')$ attains its maximum (cf. Fig. 7 in the next section). We note that the flow features obtained by using the LBE and PS methods agree well with each other, even in small scales of a few grid spacings. It should be stressed that for a strongly nonlinear system, such as the Navier–Stokes equation, a small difference in the initial conditions can grow exponentially in time. Therefore, it is remarkable that the flow fields computed from the LBE and PS methods should agree with each other so well, as shown in Figs. 1–4. The differences between the flow fields obtained by the LBE and PS methods will be further quantified in Section 4.5.

4.3. Statistical quantities

We now compare the statistical quantities of the decaying homogeneous isotropic turbulence (DHIT) obtained by using the LBE and PS methods. In Fig. 5 we first show the energy spectra $E(k, t')$ and the compensated spectra $\Psi(k, t')$. The results obtained with the LBE and PS methods with an equal time step size agree very well with each other. In fact, they show no visible difference in the spectra. If the compensated spectra is rescaled to $\Psi(k\eta, t')$, it can be shown that when $k\eta > 2$, i.e., in small scales, the compensated spectra $\Psi(k\eta, t')$ collapse to a single curve which is time independent, as expected [1].

To quantify the differences between the results obtained from different methods, we compute the following difference between the spectra $E(k, t')$:

$$\Delta E(k, t') = \|E_1(k, t') - E_2(k, t')\|, \qquad (30)$$

where the subscripts "1" and "2" denote different methods. We show the results of $\Delta E(k, t')$ for the LBE vs. PS1 (left) and PS1 vs. PS2 (right) in Fig. 6. Clearly $\Delta E(k, t')$ for LBE vs. PS1 is very similar to that for PS1 vs. PS2, as shown in Fig. 6. Also, the differences of the spectra $\Delta E(k, t')$ are very similar to the spectra $E(k, t')$ themselves.

We next show the results of the normalized total kinetic energy $K(t')/K_0$ and the normalized dissipation rate $\varepsilon(t')/\varepsilon_0$ with $Re_\lambda \approx 24.35$ in Fig. 7. Although invisible in the figure, the LBE and PS results do differ to each other. To quantify the differences in

$K(t')$ and $\varepsilon(t')$ obtained from two methods, we compute the relative differences:

$$\Delta K(t) = \frac{K'(t) - K'_*(t)}{K'_*(t)}, \qquad \Delta\varepsilon(t) = \frac{\varepsilon'(t) - \varepsilon'_*(t)}{\varepsilon'_*(t)}, \qquad (31)$$

where $K'_*(t)$ and $\varepsilon'_*(t)$ are the reference solutions obtained by the PS method with the time step size $\delta t'$ equal to that of the LBE method; $K'(t) := K(t)/K_0$ and $\varepsilon'(t) := \varepsilon(t)/\varepsilon_0$ so that $K'(0) = 1$ and $\varepsilon'(0) = 1$, and $\Delta K(0) = 0$ and $\Delta\varepsilon(0) = 0$. The results of $\Delta K(t')$ and $\Delta\varepsilon(t')$ for both the LBE vs. PS methods (LBE vs. PS1) and the PS method with two different time step sizes (PS2 vs. PS1) are shown in Fig. 8, along with the normalized rms velocity divergence $\Theta'(t')/\omega_0$, where $\omega_0 := \langle\omega_0 \cdot \omega_0\rangle^{1/2}$ is the rms value of the initial vorticity field ω_0. The relative differences $\Delta K(t')$ and $\Delta\varepsilon(t')$ between the LBE and PS methods (LBE vs. PS1) increase very rapidly in an initial period of time $t' < 1.0$, then they seem to slowly approach some asymptotic states. The rapid initial growths observed in both $\Delta K(t')$ and $\Delta\varepsilon(t')$ for LBE vs. PS1 seem to be caused by the rapid increase of the velocity divergence in the LBE simulations. Although the initial velocity field $\boldsymbol{u}_0$ is divergence free, Θ' rapidly increases to a maximum value in a very short period of time initially, then decays exponentially. The relative differences $\Delta K(t')$ and $\Delta\varepsilon(t')$ for the PS method with two different time steps (PS1 vs. PS2) are about one to two orders of magnitudes smaller than their counterparts for the LBE vs. PS methods, and they exhibit some irregular oscillations of large magnitudes, which could be due to the initial conditions.

It is known that after an initial time, the total kinetic energy and the dissipation rate decay in time as

$$K(t)/K_0 \sim [(t - t_0)/\tau_0]^{-n}, \qquad \varepsilon(t)/\varepsilon_0 \sim [(t - t_0)/\tau_0]^{-(n+1)}, \qquad (32)$$

where $\tau_0 := K_0/\varepsilon_0$ is the turbulence turnover time and t_0 is a reference time. Therefore, we can compute the decay exponent n from $K(t)/K_0$ and $\varepsilon(t)/\varepsilon_0$:

$$n_K(t_i) = \frac{\ln K(t_i) - \ln K(t_{i+1})}{\ln(t_{i+1} - t_0) - \ln(t_i - t_0)},$$
$$n_\varepsilon(t_i) + 1 = \frac{\ln \varepsilon(t_i) - \ln \varepsilon(t_{i+1})}{\ln(t_{i+1} - t_0) - \ln(t_i - t_0)}, \qquad (33)$$

where t_i and t_{i+1} are two different times. We assume $t_0 = 0$ in the above formulas to calculate the decay index n. Both $K(t)$ and $\varepsilon(t)$ are given at every 40 time steps with $\delta t' := 2\pi/N\tau_0$. The exponents of K/K_0 and $\varepsilon/\varepsilon_0$ are shown in the left of Fig. 9. The exponents computed from the LBE data oscillate rapidly about the values obtained from the PS data, which are smooth. After applying a three-point averaging several times, the high-frequency oscillations disappear and the exponents computed from the LBE data still oscillate, but with much smaller magnitudes and in much lower frequencies. The smoothed exponents obtained from LBE data agree with the PS exponents, except for the oscillations. The slow oscillations are due to acoustic waves in the LBE simulation, and the fast ones are the higher-order harmonics of the acoustic wave. The detailed analysis of these oscillations is deferred to Section 4.4.

The range of the decaying exponent n_K of the kinetic energy $K(t')$ varies between 1.6 and 2.4, and monotonically increases after $t' \approx 10.0$, as shown in Fig. 9. This is consistent with theory [45]. There are two distinctive stages of decaying process in homogeneous isotropic turbulence: the first one is the relaxation to a state of statistical equilibrium, and the second one is the final stage of decay dominated by viscous effect. When the flow is in the relaxed state, the decaying exponent n_K is given by:

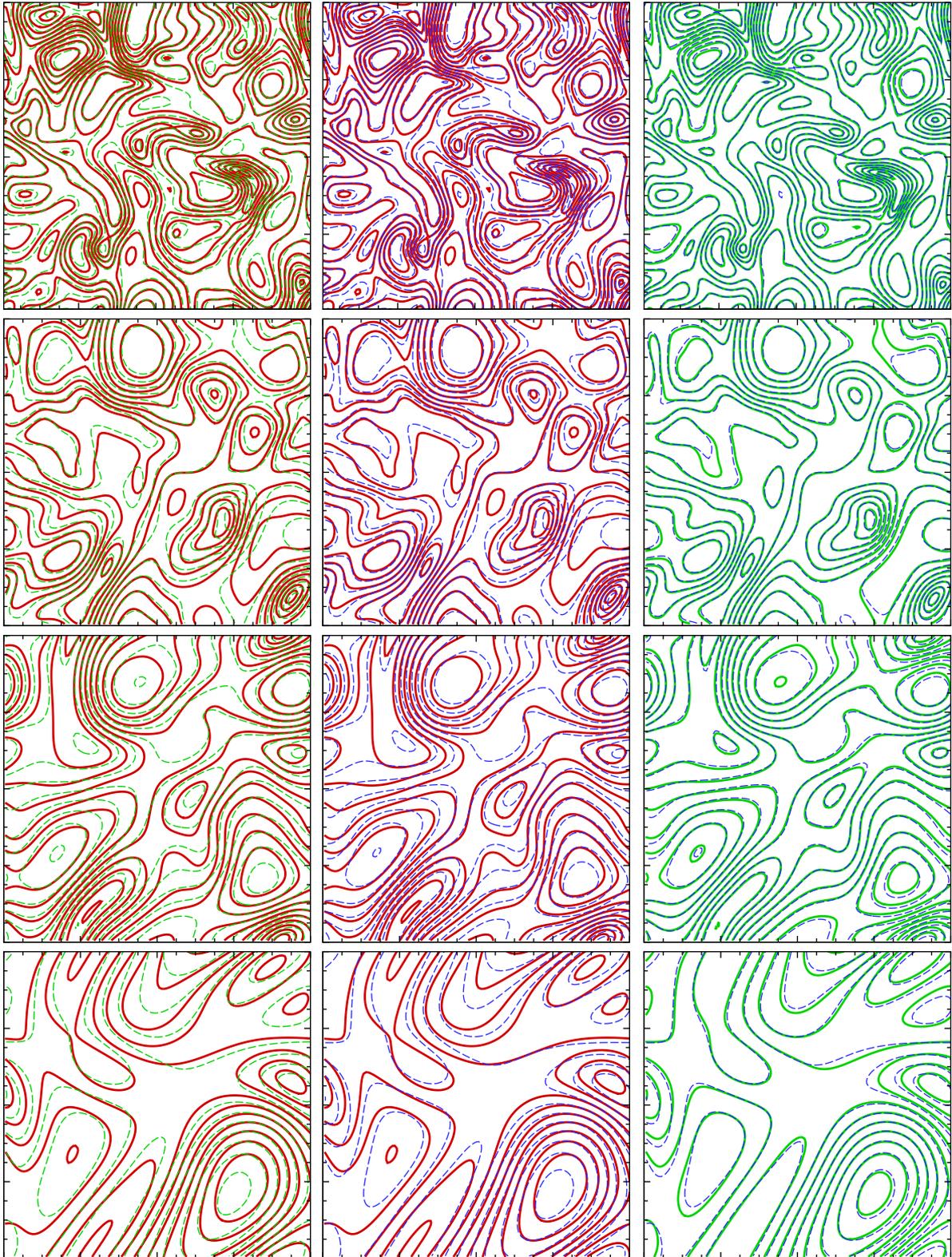$$n_K = \begin{cases} \frac{2(n+1)}{(n+3)}, & n < 4, \\ \frac{2(n+1+\delta)}{(n+3)}, & n \geqslant 4, \end{cases} \qquad (34)$$

Fig. 1. Evolution of velocity field with $Re_\lambda \approx 24.35$ and $N^3 = 128^3$. Contours of $\|\boldsymbol{u}\|/u'_0$ on the plane $z = \pi$. Left column: LBE (thick red lines) vs. PS1 (thin dashed green lines) with equal $\delta t'$; center column: LBE (thick red lines) vs. PS2 (thin dashed blue lines) with $\delta t'_{LBE} = 3\delta t'_{PS}$; and right column: PS1 (thick green lines) vs. PS2 (thin dashed blue lines). From top to bottom: $t' = 4.048169, 8.095571, 16.18959$, and 29.94941. (For interpretation of the references to colour in this figure legend, the reader is referred to the web version of this article.)

where both n and δ are determined by the asymptotic properties of the initial energy spectrum:

$$\lim_{k \to 0} E(k, t = 0) = A_0 k^n, \tag{35a}$$

$$\lim_{t \to \infty} A_0 = t^{-\delta}. \tag{35b}$$

It is observed that the effect of δ on n_K is rather weak (ca. 2%) [45]. In the final stage of decay,
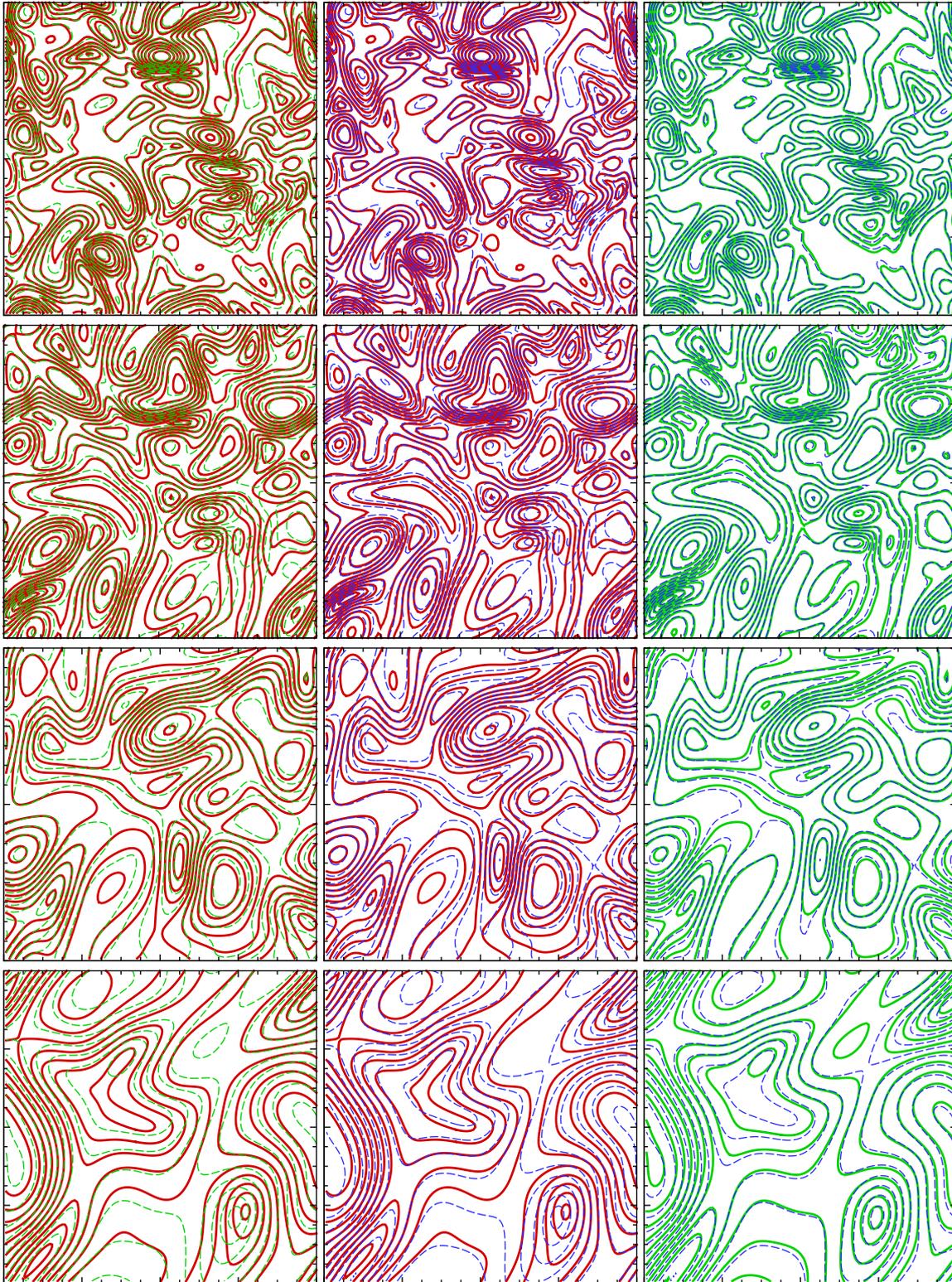
Fig. 2. Evolution of the vorticity field with $Re_{\lambda} \approx 24.35$. Contours of $\|\omega\|L/u_0'$ on the plane $z = \pi$. Similar to Fig. 1.

$$n_K = \frac{1}{2}(n + 1). \tag{36}$$

We use $n = 4$ here, as given by Eq. (17), thus $n_K \approx 10/7 \approx 1.43$ for the relaxed state and $n_K = 5/2 = 2.5$ for the final state. The results of $n_K(t')$ in Fig. 9 show that flow does go through a nonlinear relaxation and approaches to the final state of decay, as n_K becomes close to 2.5 from below. Given the significant difference between the two methods, it is remarkable that $n_K(t')$'s computed from both simulations agree so well with each other.

We compare the rms pressure fluctuation $\delta p'$ obtained by the LBE and PS methods in Fig. 10(left). While the general feature of the rms pressures obtained by the LBE and PS methods are similar,
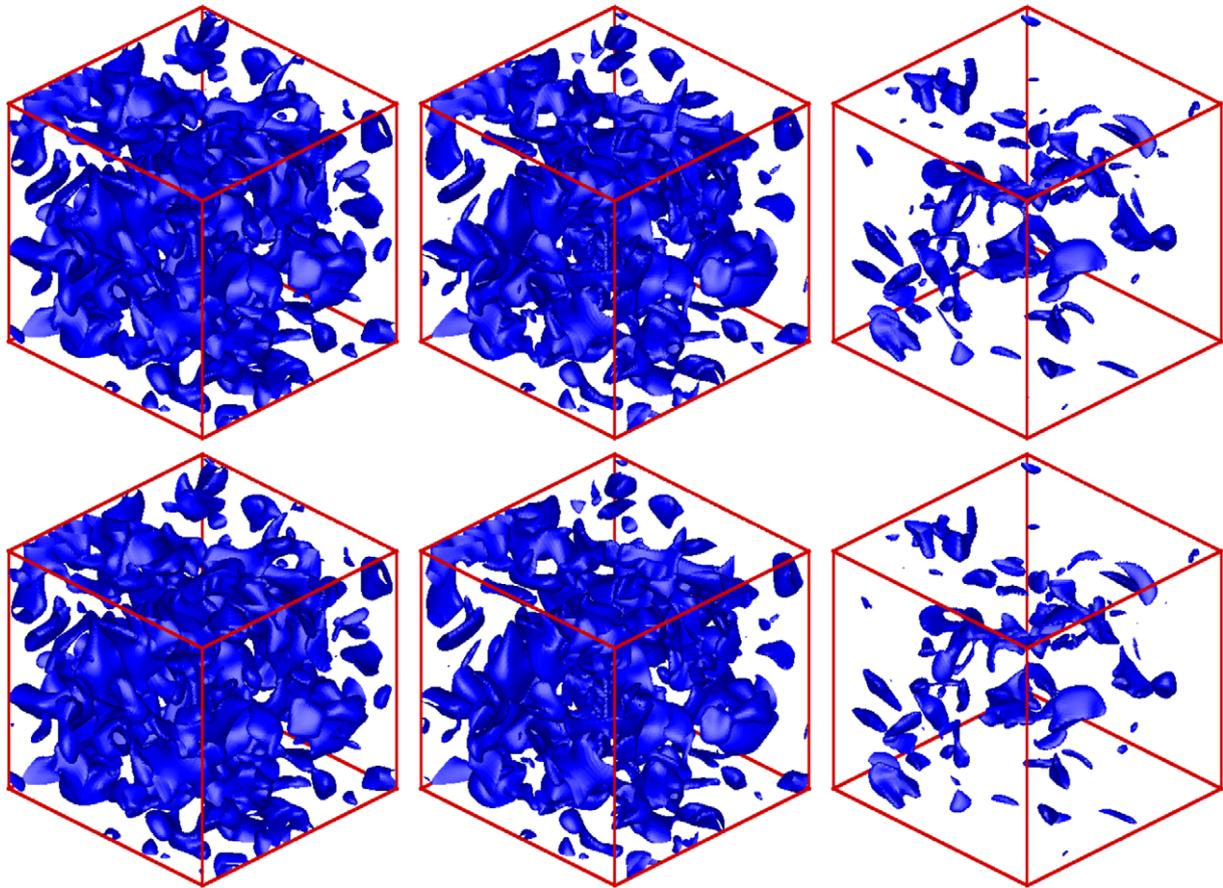
Fig. 3. Evolution of velocity magnitude iso-surface $\|\boldsymbol{u}\|/u_0' = 2.0$. $\mathrm{Re}_\lambda \approx 24.35$ and $N^3 = 128^3$. From left to right: $t' = 0.1348$, 0.2359, and 0.5730. LBE (top row) vs. PS (bottom).

their quantitative differences are considerable. First, the LBE result is oscillatory because of the acoustic waves in the system, which are absent in the PS simulations. And second, the LBE result decays slightly faster than the PS one initially, which is not visible in the figure. There are at least two obvious contributing factors responsible for the differences between the LBE and PS pressure fluctuation. First and foremost, the LBE method does not solve the Poisson equation for the pressure p, which evolves as density fluctuations through the equation of state. The initial pressure fields are not identical in the LBE and PS methods, while the initial velocity fields are identical apart from an overall scaling factor. Nevertheless, we do find that the initial rms pressure fluctuations $\delta p_0'$ in both the LBE and PS simulations are very close to each other; they differ by less than 0.7%. Second, the LBE method has a non-zero bulk viscosity ζ which is merely a numerical artifact. The bulk viscosity ζ in the LBE method affects the attenuation of acoustic waves in the system and directly contributes to the dissipation of the pressure fluctuations. Because the LBE method does not solve the Poisson equation and cannot enforce the divergence-free condition for the velocity field as in the PS method, the divergence of the velocity is not zero in the LBE simulations.

In Fig. 10(right) we show the pressure spectrum $P(k, t')$. For a short period of time up to $t' \approx 1.0$, the pressure spectrum $P(k, t')$ obtained by the LBE method agrees with that obtained by the PS method quantitatively. However, as time goes, the LBE result deviates more and more from the PS results for small k, that is, the LBE method does not accurately capture large-scale pressure fluctuations in simulations. It is interesting to note that the deteriorating pressure field in the LBE simulation seems to have little effect on the quality of the velocity and vorticity fields.

The skewness and flatness (or kurtosis) are the third-order and fourth-order moments of $\nabla\boldsymbol{u}$, respectively, and the skewness is related to the fourth-order derivative of the velocity field. For a second-order accurate method such as the LBE, computing higher-order velocity-derivatives can be a challenging task. In Fig. 11, we compare both the skewness and the flatness computed from $\partial_x u_x, \partial_y u_y, \partial_z u_z$ and their averaged value in the LBE and PS simulations. When $t' < 8.0$, the LBE and PS results agree well with each other, especially the averaged skewness S_u and flatness F_u, although the LBE results have high-frequency oscillations due to the acoustic waves in the system. The magnitudes of the oscillations grow in time as the velocity field decays, because numerical differentiation amplifies fluctuations; the higher the order of the derivatives, the greater the amplification. When high-frequency oscillations are filtered out by simple smoothing through averaging, the LBE results indeed agree very well with the PS results, as shown in the bottom row of Fig. 11. This indicates once again that the LBE pressure fluctuations due to the "artificial" compressibility do not adversely affect the averaged quantities in the simulation.

4.4. Acoustic oscillation in LBE results

One salient distinction between the LBE and PS methods is that the former is (weakly) compressible while the latter is incompressible. In the LBE method, density fluctuations are intrinsic. Also, the speed of sound is very slow, $c_s = \left(1/\sqrt{3}\right) c$ ($c := \delta x/\delta t$). We will show that intrinsic density fluctuations in the LBE method are responsible for the oscillations observed in various statistical quantities we show in the previous section.
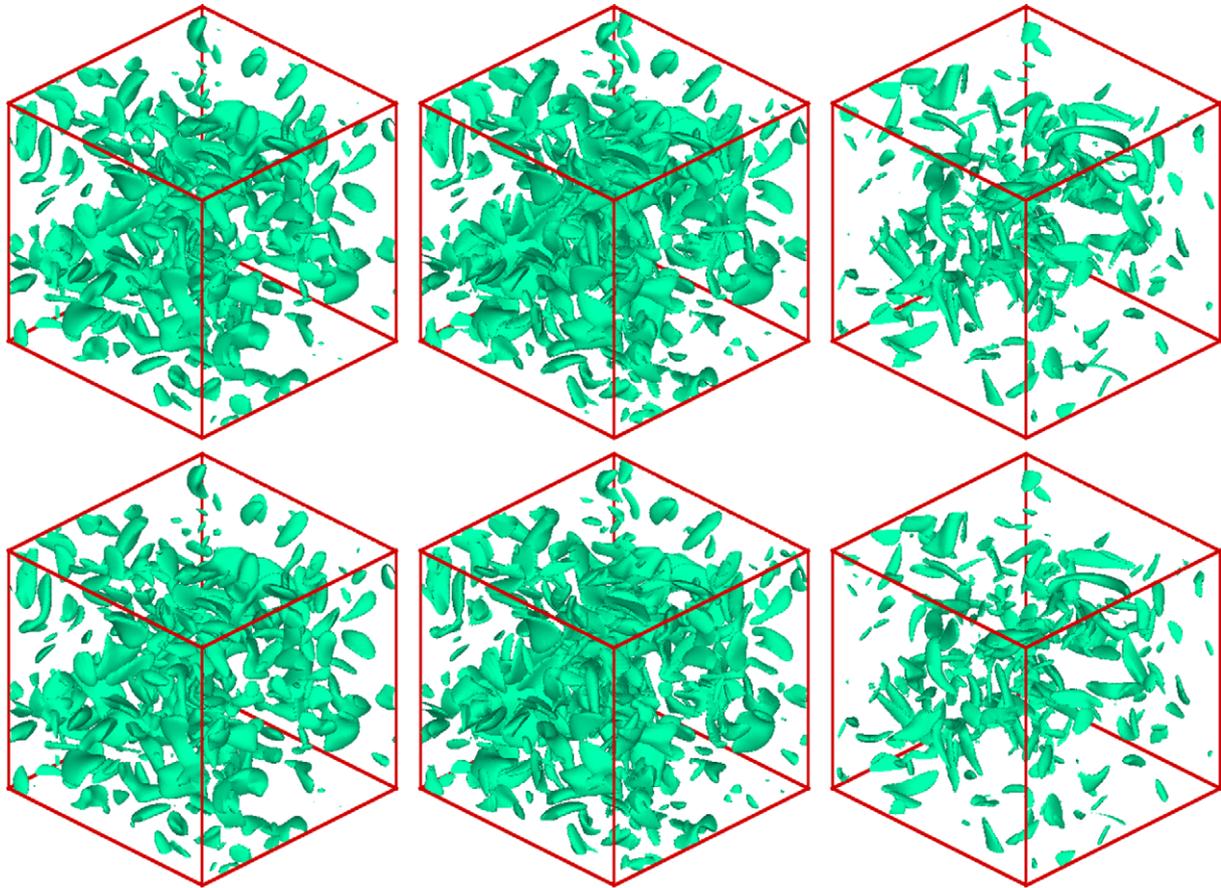
Fig. 4. Evolution of vorticity magnitude iso-surface $\|\omega\|L/u'_0 = 13.0$. $Re_\lambda \approx 24.35$ and $N^3 = 128^3$. From left to right: $t' = 0.1348$, 0.2359, and 0.5730. LBE (top row) vs. PS (bottom).
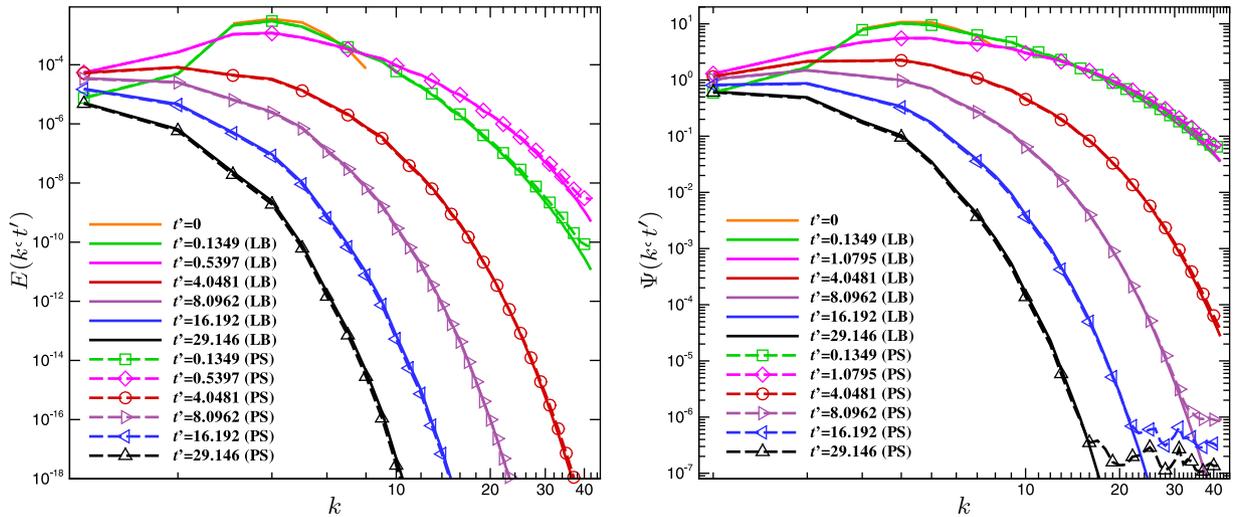

Fig. 5. The energy spectra $E(k, t')$ (left) and the compensated spectra $\Psi(k, t')$ (right) with $Re_\lambda \approx 24.35$ and $N^3 = 128^3$. The lines and symbols are the LBE and PS1 results, respectively.

Given the dimension of the cube is $L = 2\pi$ and the speed of sound is $c_s = \left(1/\sqrt{3}\right)c$, the period of the acoustic wave normalized by the turbulence turnover time $\tau_0 = K_0/\varepsilon_0$ is $T' = 2\pi\sqrt{3}\,\varepsilon_0/K_0$, and the normalized basic acoustic frequency is $f' := 1/T' = K_0/2\pi\sqrt{3}\,\varepsilon_0$. For the case of $Re_\lambda \approx 24.35$, the fundamental frequency of the sound wave should be about $f'_s \approx 1.3444$.

To identify the sources of oscillations in various quantities obtained by the LBE method, we carry out the following analysis. First, an interested quantity is decomposed into a smooth slow-varying component, which can be obtained by, e.g., local averaging, and a fast-oscillating component with zero mean value over time. Then the FFT is applied to compute the power spectrum of the fast-oscillating component in the frequency domain f'.
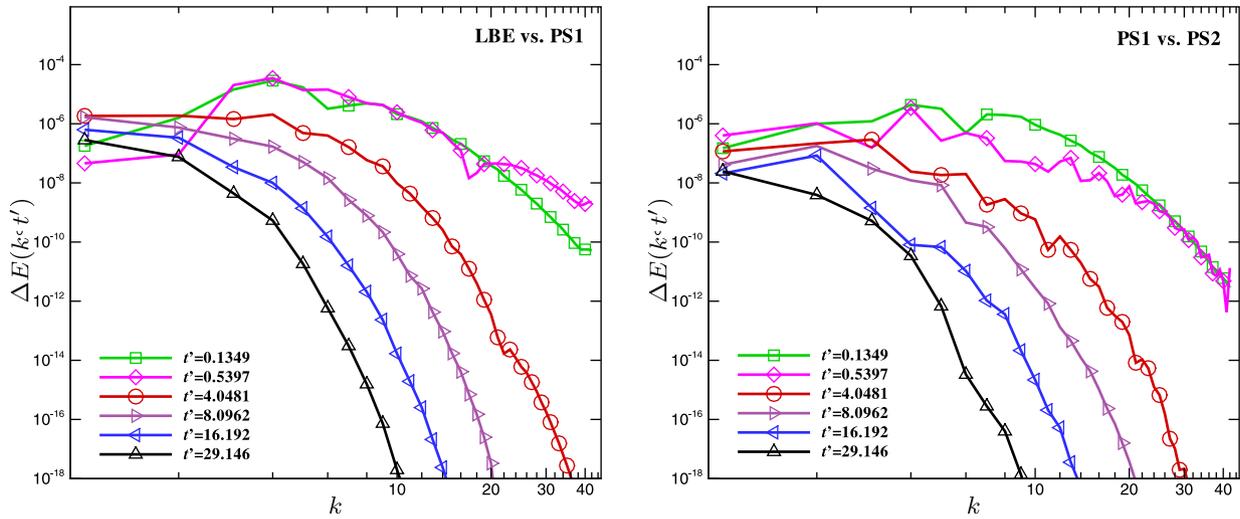
Fig. 6. The energy spectra difference $\Delta E(k, t')$ with $\mathrm{Re}_\lambda \approx 24.35$ and $N^3 = 128^3$. Left: LBE vs. PS1, corresponding to the results in Fig. 5, and right: PS1 vs. PS2.
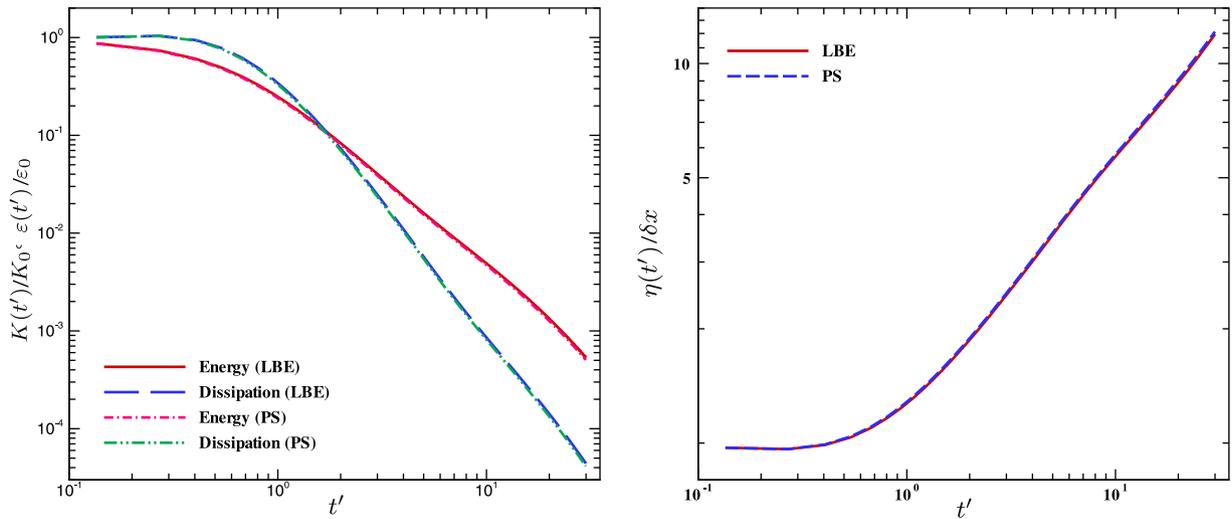
Fig. 7. Evolution of the normalized total kinetic energy $K(t')/K_0$ and the normalized dissipation rate $\varepsilon(t')/\varepsilon_0$ (left) and the normalized Kolmogorov length $\eta(t')/\delta x$ (right) with $\mathrm{Re}_\lambda \approx 24.35$ and $N^3 = 128^3$. The LBE vs. PS method with an equal $\delta t'$.
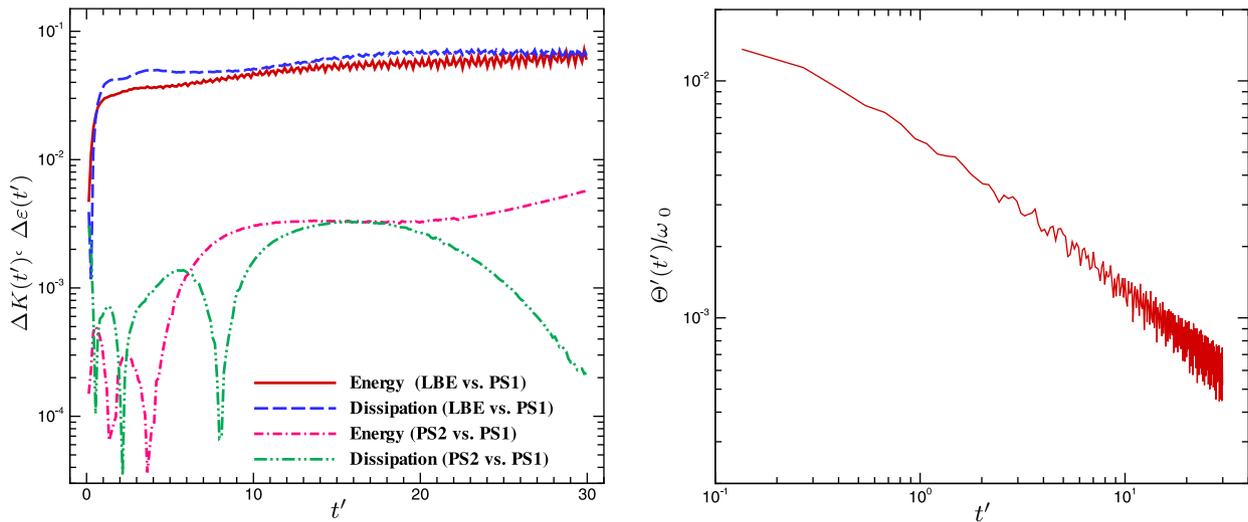
Fig. 8. The evolution of the relative differences $\Delta K(t')$ and $\Delta \varepsilon(t')$ (left) and the normalized rms velocity divergence $\Theta'(t')/\omega_0$ (right) in the LBE simulation.
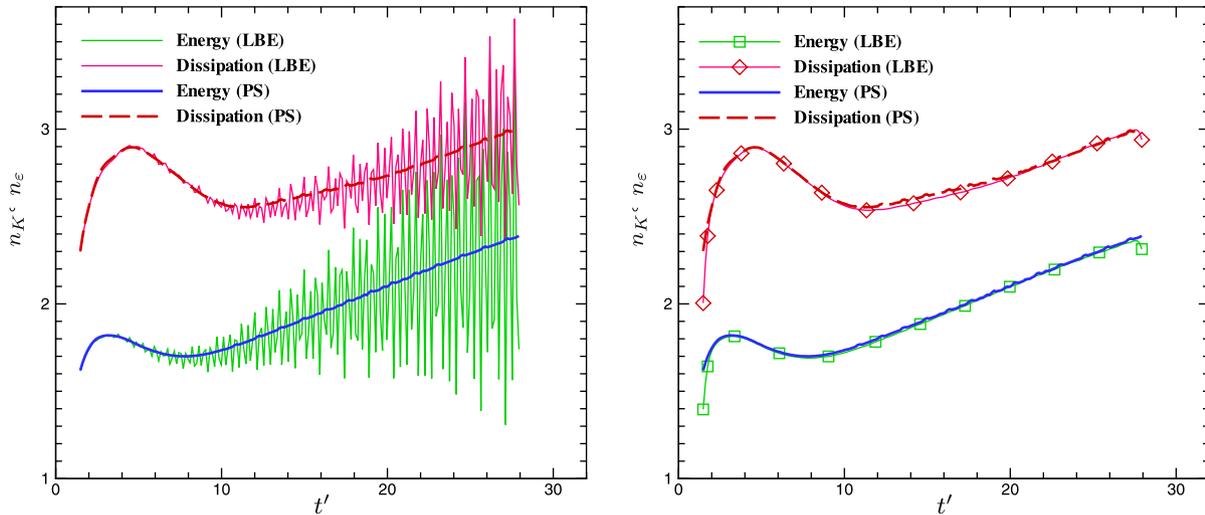
Fig. 9. Decaying exponents n_K and n_ε computed from $K(t')/K_0$ and $\varepsilon(t')/\varepsilon_0$, respectively, corresponding to Fig. 7. Left: the results computed from Eq. (33) and right: the LBE results smoothed by local averaging.
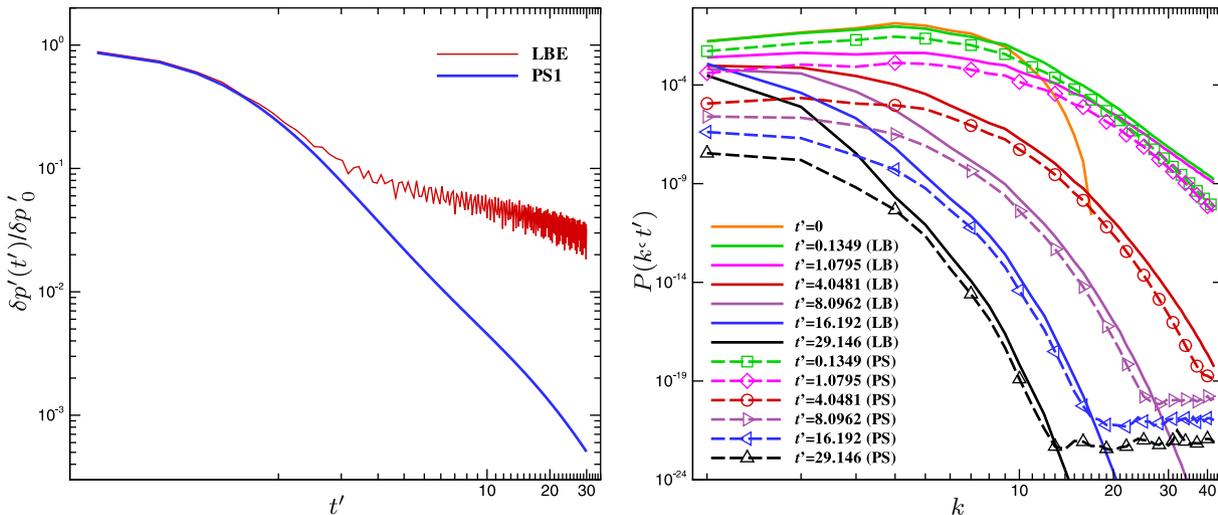
Fig. 10. The rms pressure fluctuation $\delta p'(t')/\delta p_0'$ (left) and the pressure spectra $P(k, t')$ (right), LBE vs. PS1.

We first show in Fig. 12 the power spectra of fluctuations of the decay exponent n computed from the total energy $K(t')$ and the dissipation rate $\varepsilon(t')$ by using the finite-difference formulas (33), corresponding to Fig. 9(left). The first and second peaks of both $\hat{n}_K(f')$ and $\hat{n}_\varepsilon(f')$ are $f' \approx 1.3316$ and 2.6632, respectively. The first peak corresponds to the fundamental frequency f_s' of the acoustic wave, and the second one to the second harmonic frequency $2f_s'$. The second harmonic is much more intense than the fundamental one because both $K(t')$ and $\varepsilon(t')$ are related to $\boldsymbol{u} \cdot \boldsymbol{u}$. The spectra in Fig. 12 clearly show that the acoustic wave in the LBE simulation is responsible for the oscillations in n_K and n_ε of Fig. 9(left).

We next show in Fig. 13 the power spectra of oscillating components of the rms pressure fluctuation $\delta p'(t')$ and the rms velocity divergence $\Theta'(t')$. Both these spectra are very much similar to the previous ones, for they are also related to $\boldsymbol{u} \cdot \boldsymbol{u}$. It is interesting to note that the strength of the fundamental frequency f_s' for the rms pressure fluctuation $\delta p'(t')$ is very weak.

Finally, we show in Fig. 14 the spectral analysis for the skewness and flatness of the LBE simulations. The spectra of the skewness and the flatness have more peaks than, for example, that of the rms pressure. There are four most prominent peaks, labeled by A, B, C and D, situated at $f_A' \approx 1.360 \approx f_s'$, $f_B' \approx 1.968$, $f_C' \approx 2.315$ and $f_D' \approx 2.750 \approx$

$2f_s'$, respectively. Clearly, f_A' and f_D' correspond to the basic and second harmonic frequencies of the acoustic wave in the system. However, it is not so clear what the other peak frequencies correspond to. We suspect that the frequency f_B' corresponds to the wave traveling along the diagonals of a plane parallel to the faces of the cube, and f_C' to the diagonals of the cube, because $f_B' \approx \sqrt{2}f_s' = 2c_s\tau_0/\sqrt{2}L$ and $f_C' \approx \sqrt{3}f_s' = 3c_s\tau_0/\sqrt{3}L$. In addition, $f' \approx f_B'/2 \approx 0.984$, $f_C'/3 \approx 0.772$ and $2f_C'/3 \approx 1.54$ can be seen in the frequency spectrum of the skewness, shown in Fig. 14 (left): the subharmonics $f_B'/2$ and $f_C'/3$ on the left of peak A are labeled as a and b, respectively; peak d, between peak A and peak B, is about $f' \approx 2f_C'/3$; and peak e, on the right of peak D, is $f' \approx 3f_B'/2$.

To definitively identify the source of oscillations in the LBE simulations, we perform the following test. Besides the accuracy, the greatest distinction between the LBE and PS methods is treatment of pressure p. The PS method solves the Poisson equation for the pressure p in $\boldsymbol{k}$-space, while the LBE method relates the pressure p to the density ρ through the equation of state $p = c_s^2\rho$, thus density fluctuations are essential in LBE simulations. To mitigate the effect of density fluctuations, we alter the LBE algorithm as follows. Instead of the simple advection–collision algorithm, we apply an iterative algorithm [44] to consistently solve the Poisson equation
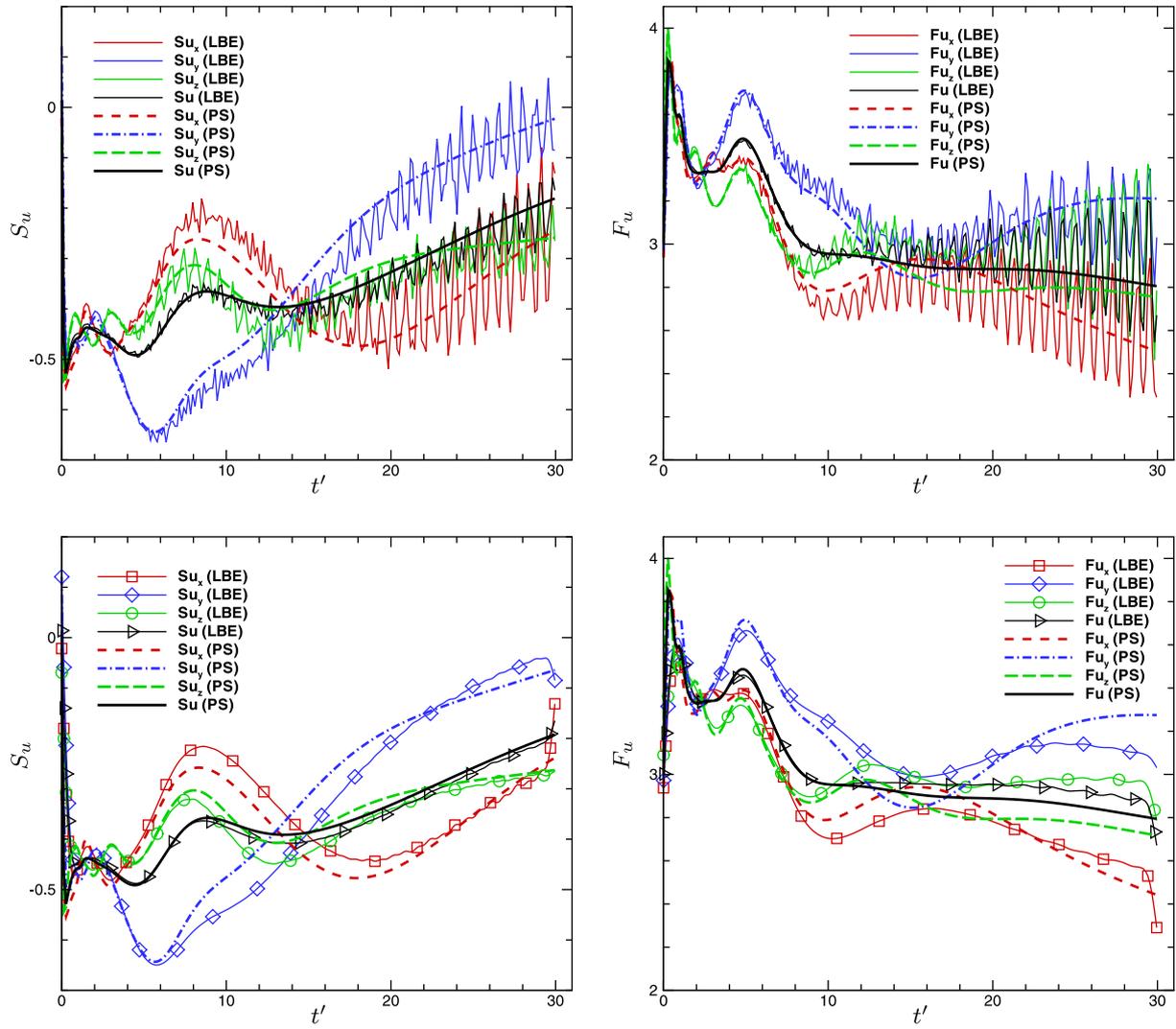
Fig. 11. The skewness (left) and the flatness (right) with $Re_\lambda \approx 24.35$ and $N^3 = 128^3$. The LBE (thin lines) vs. PS1 (thick patterned lines). In the bottom row, the LBE data (thin line with symbols) have been smoothed.
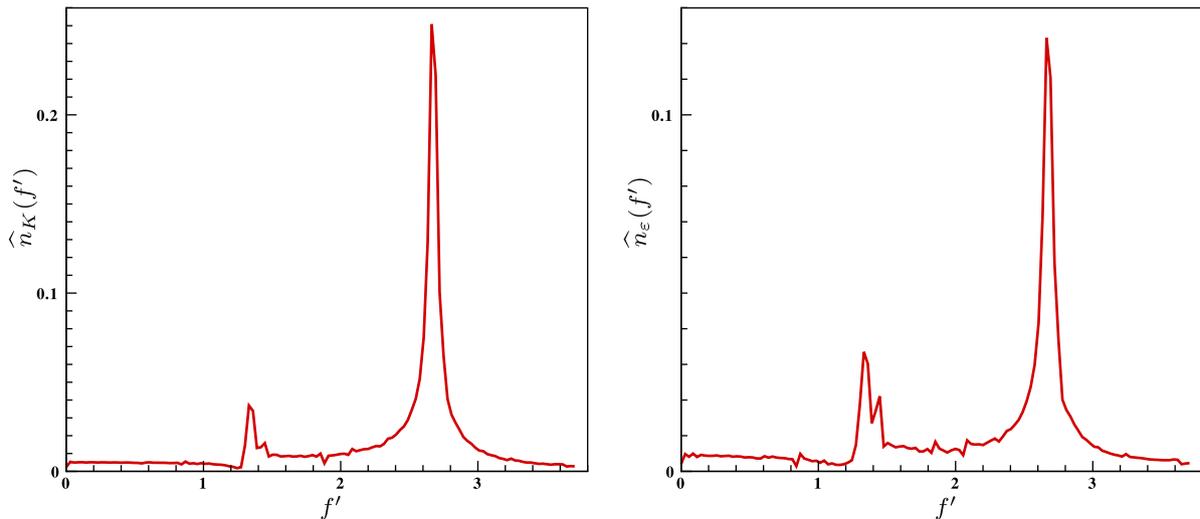

Fig. 12. The power spectra of the fluctuations in the decay exponent $n(t')$ computed from the total energy $K(t')$ (left) and the dissipation rate $\varepsilon(t')$ (right) of the LBE simulation, corresponding to the data in Fig. 9 (left). $Re_\lambda \approx 24.35$ and $N^3 = 128^3$.
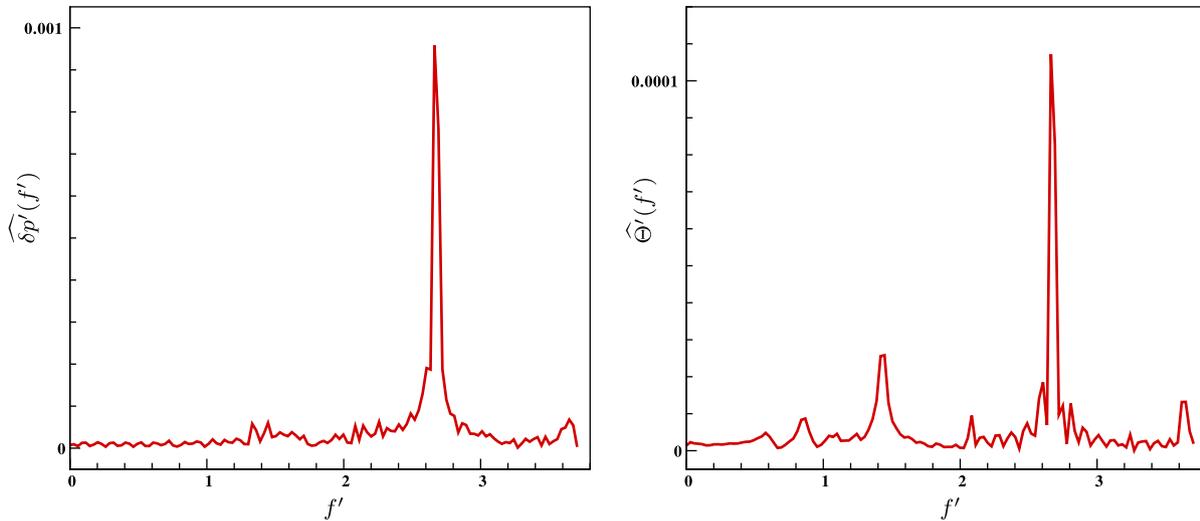
Fig. 13. The power spectra of the rms pressure fluctuation $\widehat{\delta p'}(f')$ (left) and the rms velocity divergence $\widehat{\Theta'}(f')$ (right), corresponding to Fig. 10 (left) and Fig. 8, respectively. $Re_\lambda \approx 24.35$ and $N^3 = 128^3$.
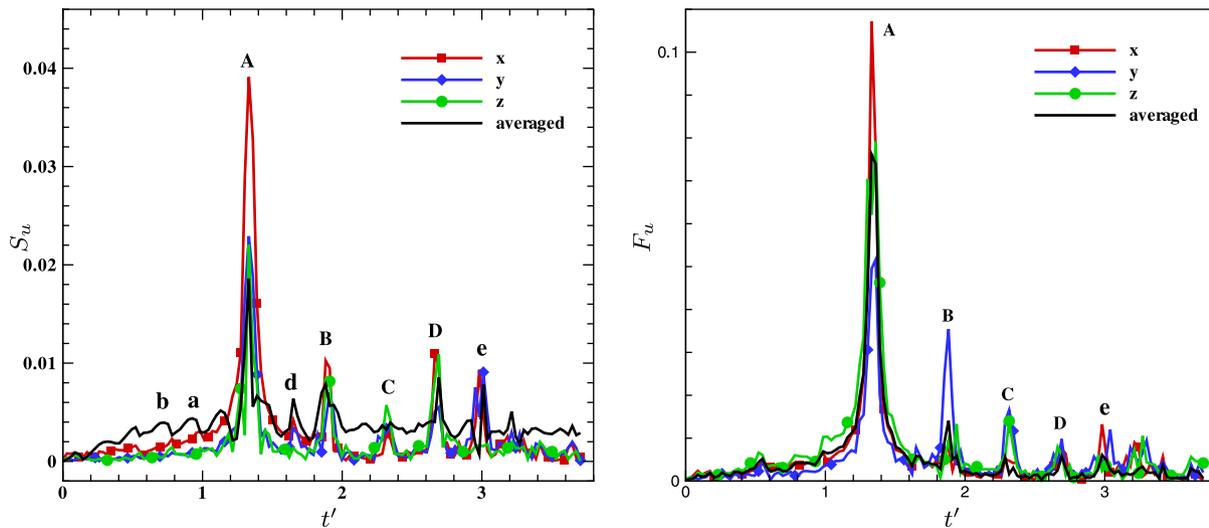
Fig. 14. The power spectra of the oscillating components of the skewness (left) and the flatness (right), corresponding to the data of Fig. 11 left and right, respectively. $Re_\lambda \approx 24.35$ and $N^3 = 128^3$.

after each collision step. That is, after each advection–collision step, the local velocity field $\boldsymbol{u}(\boldsymbol{x}_j, t_i)$ is kept unchanged while the collision step is repeated for, say, 20 times, to obtain the density $\rho(\boldsymbol{x}_j, t_i)$. Then the advection–collision is repeated again. The result for the skewness $S_u(t')$ obtained in this test is shown in Fig. 15. In Fig. 15, we show the skewness $S_u(t')$ obtained by the PS and LBE method, corresponding to the data shown in Fig. 11(left), and by the advection–collision-iteration scheme. Clearly, the oscillations in $S_u(t')$ have been completely eliminated by the advection–collision-iteration scheme. This conclusively proves that density fluctuations are the source of the oscillations in the statistical quantities obtained by using the LBE method. While the advection–collision-iteration scheme can eliminate the acoustic oscillations, the scheme is inaccurate and unstable, as indicated in Fig. 15: after $t' \approx 3.3$, the simulation diverges.

While the advection–collision-iteration scheme is useful to identify the source of oscillations in the LBE simulations, it cannot be used to reduce the oscillation because it is neither accurate nor stable, as shown by the results of Fig. 15. Given the compressible nature of the LBE method, our options to reduce the acoustic effect

in LBE simulations are rather limited. We do not want to use a smaller Mach number because that effectively reduces the CFL number and hence the efficiency. Since the equilibria are related to the second-order Taylor expansion of the Maxwellian in $\boldsymbol{u}$ [16,17], we can consider using a higher-order expansion in $\boldsymbol{u}$ for the equilibria. We test the equilibria including the terms of $O(u^3)$, and results are shown in Fig. 16. In Fig. 16 we compare the skewness $S_u(t')$ and the flatness $F_u(t')$ computed from the LBE scheme with the second-order and third-order equilibria. Clearly, the third-order equilibria reduce the magnitude of oscillations in both S_u and F_u only very little.

4.5. Effects due to the viscosity or the Reynolds number

To investigate the effect of the viscosity ν or the Reynolds number on the results obtained from the LBE and PS methods, we conduct simulations with different values of the viscosity ν, and fixed mesh size $N^3 = 128^3$ and the initial energy spectrum $E_0(k)$, resulting in different Taylor micro-scale Reynolds numbers. The values of
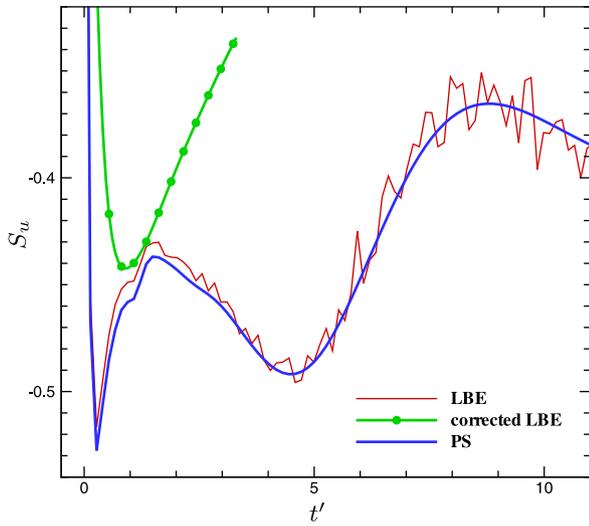
Fig. 15. The oscillations due to the acoustics in the LBE simulation. The skewness $S_u(t')$ computed by using the LBE (thin line), PS (thick line) and the LBE with advection–collision-iteration scheme (line with symbols).

Re_λ, ν and the normalized initial Kolmogorov length scale $\eta_0/\delta x$ used in the simulations are given in Table 2.

It is important to note that with the initial spectrum given by Eq. (17), the required resolution in the simulation is explicitly specified by k_b. However, as the flow evolves, all the modes in $\boldsymbol{k}$ space are filled immediately. The dissipation rate $\varepsilon(t)$ will reach a maximum before it decays monotonically. The Kolmogorov scale $\eta(t)$ will attain a minimum when $\varepsilon(t)$ reaches its maximum. The minimum of $\eta(t)$ is not too far from its initial value η_0. For this reason η_0 is given in Table 2 as a reference value.

We first investigate the Reynolds-number dependence of the difference between instantaneous flow fields obtained from the LBE and PS methods by comparing the flow fields with the Reynolds numbers $Re_\lambda \approx 40.67$ at $t' \approx 4.0400$ and $Re_\lambda \approx 72.37$ at $t' \approx 4.0869$. The results are shown in Figs. 17 and 18 for $Re_\lambda \approx 40.67$ and 72.37, respectively. For the case of $Re_\lambda \approx 40.67$ shown in Fig. 17, the LBE flow fields are clearly different from the PS ones, although strong correlations can still be observed, while the PS results obtained with different time step sizes still agree with each other rather well. As for the case of $Re_\lambda \approx 72.37$ shown in Fig. 18, the LBE flow fields have very little resemblance

to the PS ones. However, the flow fields obtained by the PS method with different time step sizes still exhibit a much better resemblance to each other than the fields obtained by two different methods. Clearly, the differences between the flow fields obtained with different methods or with different time step sizes increase as the Reynolds number Re_λ increases.

To quantify the difference between the flow fields obtained by using different methods, we compute the L_2-norm of the difference between two flow fields:

$$\|\delta\bar{\boldsymbol{v}}\| := \|\bar{\boldsymbol{v}}_1 - \bar{\boldsymbol{v}}_2\|, \tag{37}$$

where $\bar{\boldsymbol{v}} := \boldsymbol{v}/u_0'$, $\boldsymbol{v}$ is either the velocity or vorticity field, u_0' is the initial rms velocity, and $\bar{\boldsymbol{v}}_1$ and $\bar{\boldsymbol{v}}_2$ are flow fields obtained by methods "1" and "2", respectively. We compute the flow field differences with the five Reynolds numbers given in Table 2. Again, we compare the results obtained by the LBE method and the PS method with two different time step sizes, and the results for $\|\delta\bar{\boldsymbol{u}}(t')\|$ and $\|\delta\bar{\omega}(t')\|$ are shown in Fig. 19.

The following observations of the flow field differences can be made. First, for the velocity difference $\|\delta\bar{\boldsymbol{u}}(t')\|$, after a short initial period of time, they all appear to grow *linearly* in time. The slope of $\|\delta\bar{\boldsymbol{u}}(t')\|$, i.e., $d\|\delta\bar{\boldsymbol{u}}\|/dt'$, clearly depends on the Reynolds number Re_λ; the slope increases as Re_λ increases. It should be noted that with the resolution N^3 and time step size $\delta t'$ fixed, the velocity difference $\|\delta\bar{\boldsymbol{u}}(t')\|$ appears to saturate, as indicated in the case of LBE vs. PS method with an equal time step size $\delta t'$ (labeled as PS1 in the figure), shown in the first figure in left column of Fig. 19. The results of $\|\delta\bar{\boldsymbol{u}}(t')\|$ for $Re_\lambda \approx 65.07$ and 72.37 almost overlap with each other. However, when the results with the time step size of $\delta t'$ are compared with the results with PS method with the time step size of $\delta t'/3$ (labeled as PS2 in the figure), the velocity differences $\|\delta\bar{\boldsymbol{u}}(t')\|$ are in fact distinguishable for both cases of $Re_\lambda \approx 65.07$ and 72.37. We note that the maximum Reynolds number estimated by Eq. (27) is about $Re_{\lambda\,max} \sim 47.8$, thus both $Re_\lambda \approx 65.07$ and 72.37 exceed this maximum value of Re_λ allowed by the given resolution of $N^3 = 128^3$. In other words, when the

Table 2
The viscosity ν, the initial Taylor micro-scale Reynolds number Re_λ, and the initial Kolmogorov length scale η_0 in the simulations.

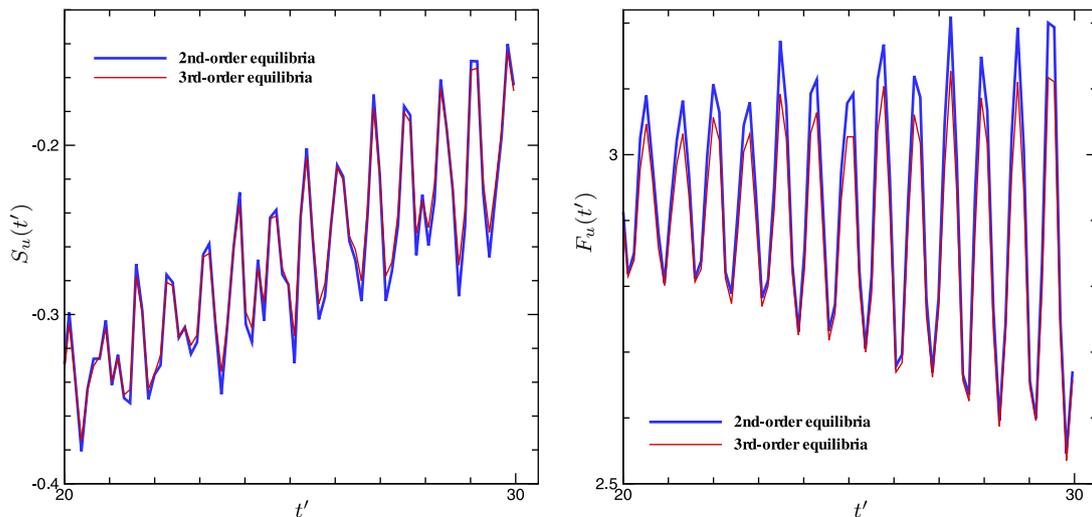| ν	1/600	1/1000	3/4000	1/1600	1/1800
Re_λ	24.35	40.67	54.23	65.07	72.37
$\eta_0/\delta x$	1.036	0.802	0.695	0.634	0.598

Fig. 16. The effect of the equilibria on the skewness $S_u(t')$ (left) and the flatness $F_u(t')$. The results with the second-order equilibria (thick blue lines) vs. that with the third-order equilibria (thin red lines). (For interpretation of the references to colour in this figure legend, the reader is referred to the web version of this article.)
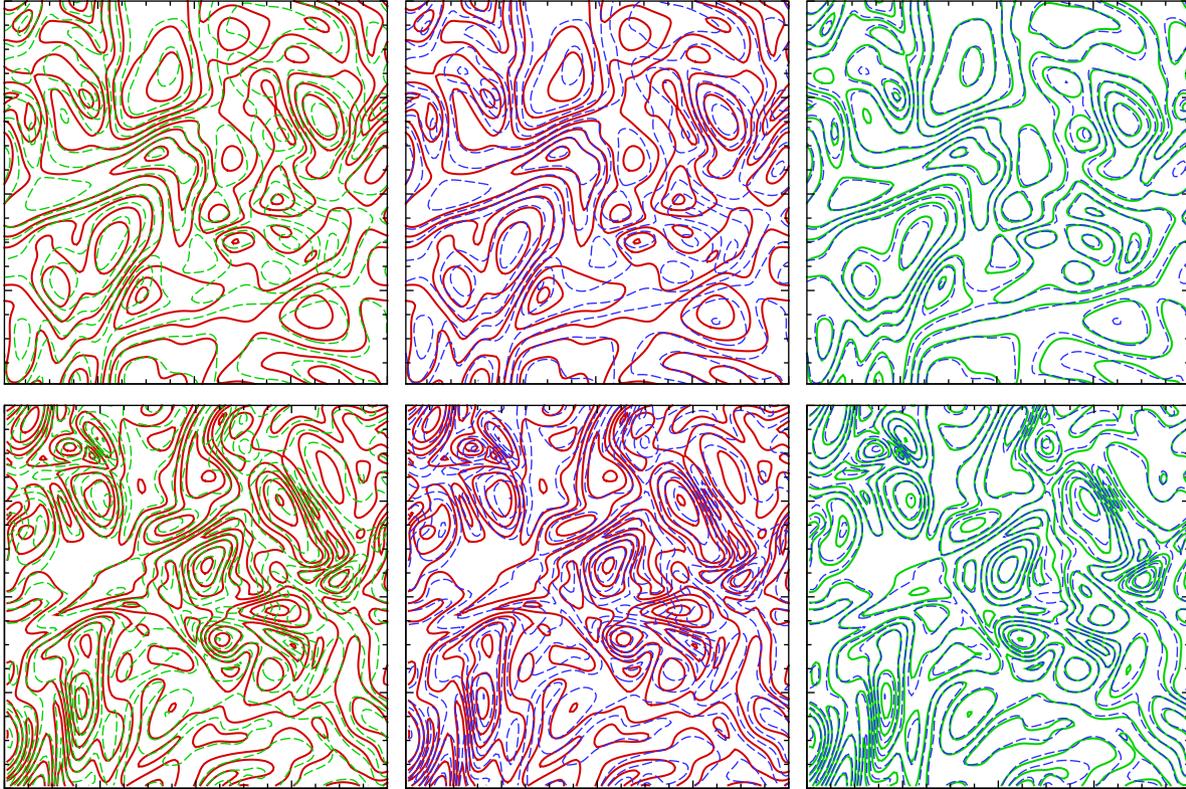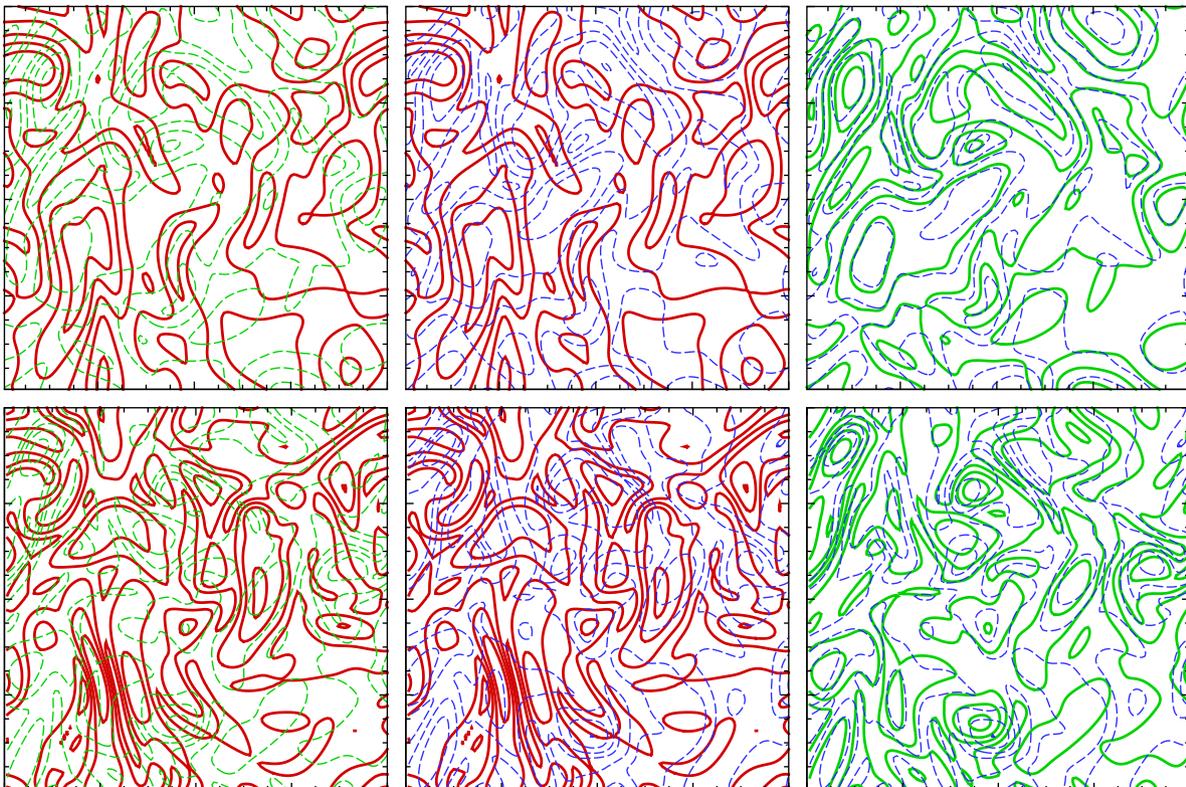
Fig. 17. Instantaneous velocity $\|\boldsymbol{u}\|/u_0'$ (top) and vorticity $\|\boldsymbol{\omega}\|L/u_0'$ (bottom) fields with $Re_\lambda \approx 40.67$ at $t' \approx 4.05$. Contours on the plane $z = \pi$. From left to right: LBE (thick red lines) vs. PS1 (thin dashed green lines), LBE (thick red lines) vs. PS2 (thin dashed blue lines), and PS1 (thick green lines) vs. PS2 (thin dashed blue lines). (For interpretation of the references to colour in this figure legend, the reader is referred to the web version of this article.)

Fig. 18. Instantaneous velocity $\|\boldsymbol{u}\|/u_0'$ (top) and vorticity $\|\boldsymbol{\omega}\|L/u_0'$ (bottom) fields with $Re_\lambda \approx 72.37$ at $t' \approx 4.05$. Contours on the xy plane $z = \pi$. From left to right: LBE (thick red lines) vs. PS1 (thin dashed green lines), LBE (thick red lines) vs. PS2 (thin dashed blue lines), and PS1 (thick green lines) vs. PS2 (thin dashed blue lines). (For interpretation of the references to colour in this figure legend, the reader is referred to the web version of this article.)

initial flow field is under-resolved, the velocity difference $\|\delta \bar{\boldsymbol{u}}(t')\|$ does not depend on the Reynolds number as strongly as when the flow is well resolved.

The evolution of the vorticity difference $\|\delta \bar{\omega}(t')\|$ behaves drastically different from the velocity difference $\|\delta \bar{\boldsymbol{u}}(t')\|$. The vorticity difference $\|\delta \bar{\omega}(t')\|$ for different methods and different time step sizes $\delta t'$ increases rapidly in an initial period of time, up to $t' \approx 2.0$, and then reaches a saturated final value depending on the Reynolds number Re_λ, as shown in the right column of Fig. 19. Clearly, the saturated value of $\|\delta \bar{\omega}(t')\|$ increases as the Rey-
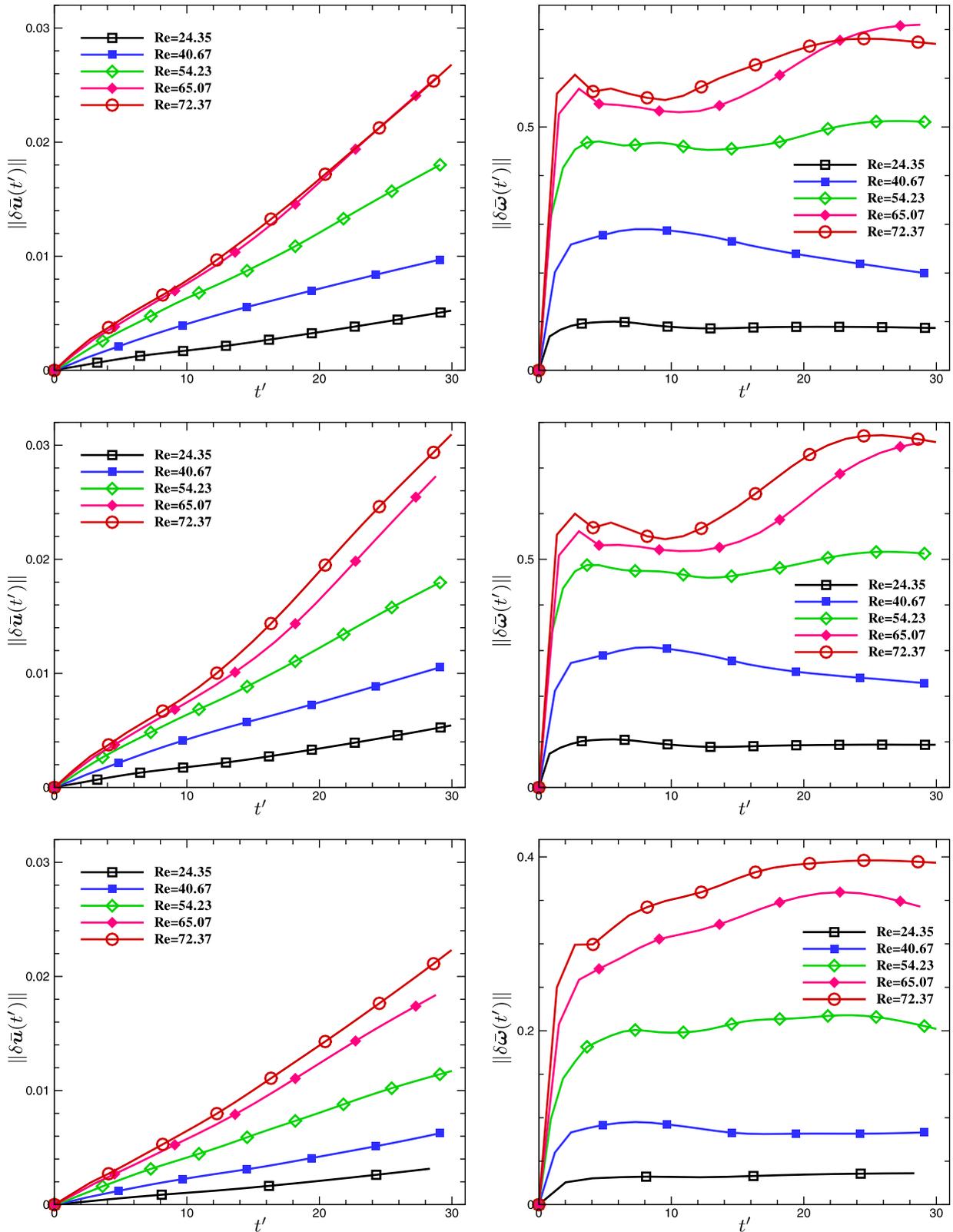
Fig. 19. Evolution of $\|\delta \bar{\boldsymbol{u}}(t')\|$ (left) and $\|\delta \bar{\omega}(t')\|$ (right). From top to bottom: LBE vs. PS1, LBE vs. PS2, and PS1 vs. PS2.

nolds number Re_λ increases, provided that the grid resolution N is sufficiently large to resolve the flow. However, when the flow is severely under-resolved, as in the cases of $Re_\lambda \approx 65.07$ and 72.37, the saturated value of $\|\delta\bar{\omega}(t')\|$ weakly depends on Re_λ. It is interesting to note that there is no obvious and *qualitative* difference in either $\|\delta\bar{u}(t')\|$ or $\|\delta\bar{\omega}(t')\|$ due to different methods or the same method with different time step sizes, the differences are only *quantitative*.

To further quantify the difference between the flow fields obtained by using difference methods, we compute the Reynolds-number dependence of the slope $d\|\delta\bar{u}(t')\|/dt'$ for the velocity difference $\|\delta\bar{u}(t')\|$. The values of $d\|\delta\bar{u}(t')\|/dt'$ are computed by using the least-square linear fit with the data of $t' \geqslant 16.0$ in Fig. 19. The results of $d\|\delta\bar{u}(t')\|/dt'$ as a function of the grid Reynolds number $Re_\lambda^* := Re_\lambda/N$ are shown in Fig. 20. Several interesting observations can be made of Fig. 20. First, it appears that the growth rate $d\|\delta\bar{u}(t')\|/dt'$, regardless of methods and time step size $\delta t'$, has an approximately linear dependence on the Reynolds number Re_λ when the flow is properly resolved by the both methods. In particular, the growth rates of $\|\delta\bar{u}(t')\|$ for the LBE vs. PS method with an equal time step size $\delta t'$ (PS1) and the LBE vs. PS method with a smaller ($\delta t'/3$) time step size (PS2), corresponding to top and middle plot in Fig. 19, respectively, are almost identical when $Re_\lambda^* := Re_\lambda/N < Re_{\lambda\,max}/N \approx 0.3655$, where the $Re_{\lambda\,max} \approx 46.784$ is estimated by using Eq. (27), thus $Re_{\lambda\,max}/N \approx 0.3655$. This suggests that when the flow is properly resolved by both methods, the difference in spatial accuracy decides the Reynolds-number dependence of the growth rate of the velocity difference $d\|\delta\bar{u}(t')\|/dt'$, while the time step size δt has little effect, although the velocity difference itself $\|\delta\bar{u}(t')\|$ is affected by both the spatial accuracy and the time step size $\delta t'$. The growth rates obtained by using the PS method with different time step sizes show a Reynolds-number dependence similar to that of LBE vs. PS method, *i.e.*, it exhibits a similar linear dependence, as shown in Fig. 20. Again, the *global* difference of flow fields computed from different methods is quantitative, rather than qualitative.

We will next show the effect of the Reynolds number Re_λ on the statistical quantities. In Fig. 21 we first show the dependence of $K(t)$, $\varepsilon(t)$, and $\eta(t)$ on the Reynolds number Re_λ. For the case of $Re_\lambda \approx 40.67$, the results of the LBE and PS methods agree with each other. They show very little differences in the figures. However, for the case of $Re_\lambda \approx 72.37$, the differences between the LBE and PS results are visible in the figures. The LBE and PS results agree only up to about $t' \approx 10$, and both the energy $K(t)$ and the dissipation rate $\varepsilon(t)$ decay slower than the corresponding PS results after $t' > 10$. We also show the relative differences $\Delta K(t')$ and $\Delta\varepsilon(t')$ in Fig. 21 for the LBE vs. PS method (LBE vs. PS1) and the PS method with two different time steps (PS2 vs. PS1). We observe that both $\Delta K(t')$ and $\Delta\varepsilon(t')$ increase as Re_λ increases, while the gaps between $\Delta K(t')$ and $\Delta\varepsilon(t')$ for both LBE vs. PS1 and PS2 vs. PS1 decrease.

Fig. 22 shows the energy spectra $E(k, t')$ and the compensated spectra $\Psi(k, t')$ for $Re_\lambda \approx 40.67$ and 72.37. For the case of $Re_\lambda \approx 40.67$, both $E(k, t')$ and $\Psi(k, t')$ computed from the two methods agree well with each other. As for the case of $Re_\lambda \approx 72.37$, some discrepancies in high wave-numbers and at late times are visible. It should be noted that, compared to the case of $Re_\lambda \approx 24.35$ shown in Fig. 5, both $E(k, t')$ and $\Psi(k, t')$ with $Re_\lambda \approx 72.37$ are rather flat at large k initially, a clear indication that the viscous sub-range is lacking as a consequence of insufficient resolution. Nevertheless, the spectra obtained by the two methods still maintain good agreement with each other.

Fig. 23 shows the rms pressure fluctuation $\delta p'(t')/\delta p_0'$ and the pressure spectrum $P(k, t')$ for $Re_\lambda \approx 40.67$ and 72.37. The rms pressure fluctuations $\delta p'(t')/\delta p_0'$ computed from the LBE method with $Re_\lambda \approx 40.67$ and 72.37 start to deviate from the PS results at $t' \approx 1.0$ and 0.4, respectively. Except for a very short initial period

of time, the LBE pressure spectra $P(k, t')$ differ from the PS pressure spectra significantly, especially at low wave-numbers.

Finally, we show in Figs. 24 and 25 the skewness and flatness, respectively, at $Re_\lambda \approx 40.67$ and 72.37. At $Re_\lambda \approx 40.67$, both the skewness and flatness computed with the LBE method agree with their PS counterparts only in a short initial period of time $t' < 2.0$, while the results of both the skewness and flatness computed from the PS method with different time step sizes (PS1 and PS2) agree very well with each other in the entire period of time of the simulation. As the Reynolds number increases to $Re_\lambda \approx 72.37$, the initial period of time in which the LBE results of the skewness and the flatness agree with the PS results is shorten to $t' < 0.5$. The same is also true for the results obtained by using the PS method with different time step sizes. Nevertheless, the LBE results still agree with the PS results qualitatively.

Based on the observations made above, we can conclude that the flow fields computed with the LBE method agree well with those computed with the PS method when the initial flow field is properly resolved by both methods. Furthermore, the difference between the flow fields computed with the LBE and PS methods is qualitatively similar to that between the flow fields computed with the PS method with different time step sizes. Clearly, as the viscosity decreases and the Reynolds number increases with a fixed grid resolution N^3, the flow may not be adequately resolved. The effect due to inadequate resolution is more severe in the instantaneous flow fields than in the statistical quantities. In fact, except the rms pressure and the pressure spectrum, all other statistical quantities computed by using the LBE method are acceptable even when the flow is under-resolved.

4.6. Computational efficiency

Finally, we compare the computational efficiency of the LBE and PS methods. For efficiency test we use a fixed mesh size $N^3 = 128^3$ and 1000 time steps. The CPUs are the Intel Xeon 5160 "Woodcrest" chips (4 cores) running at 3.0 GHz with 4MB shared level 2 cache per dual core. With both collision and advection combined in one step, the D3Q19 LBE model is about 2.58 times faster than the PS method when four CPUs are used. From Fig. 26, we can see that the PS method scales very well up to 32 CPUs with a fixed system size $N^3 = 128^3$, while the LBE method does not. The reason is the following. As a second-order method, the LBE requires much
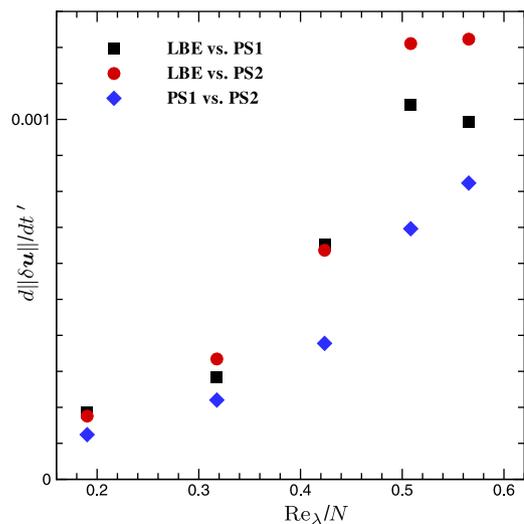

Fig. 20. The Reynolds-number dependence of the growth rate for the velocity difference in time, $d\|\delta u\|/dt'$, with different methods and time step sizes. We use the grid Reynolds number $Re_\lambda^* := Re_\lambda/N$ for this figure.
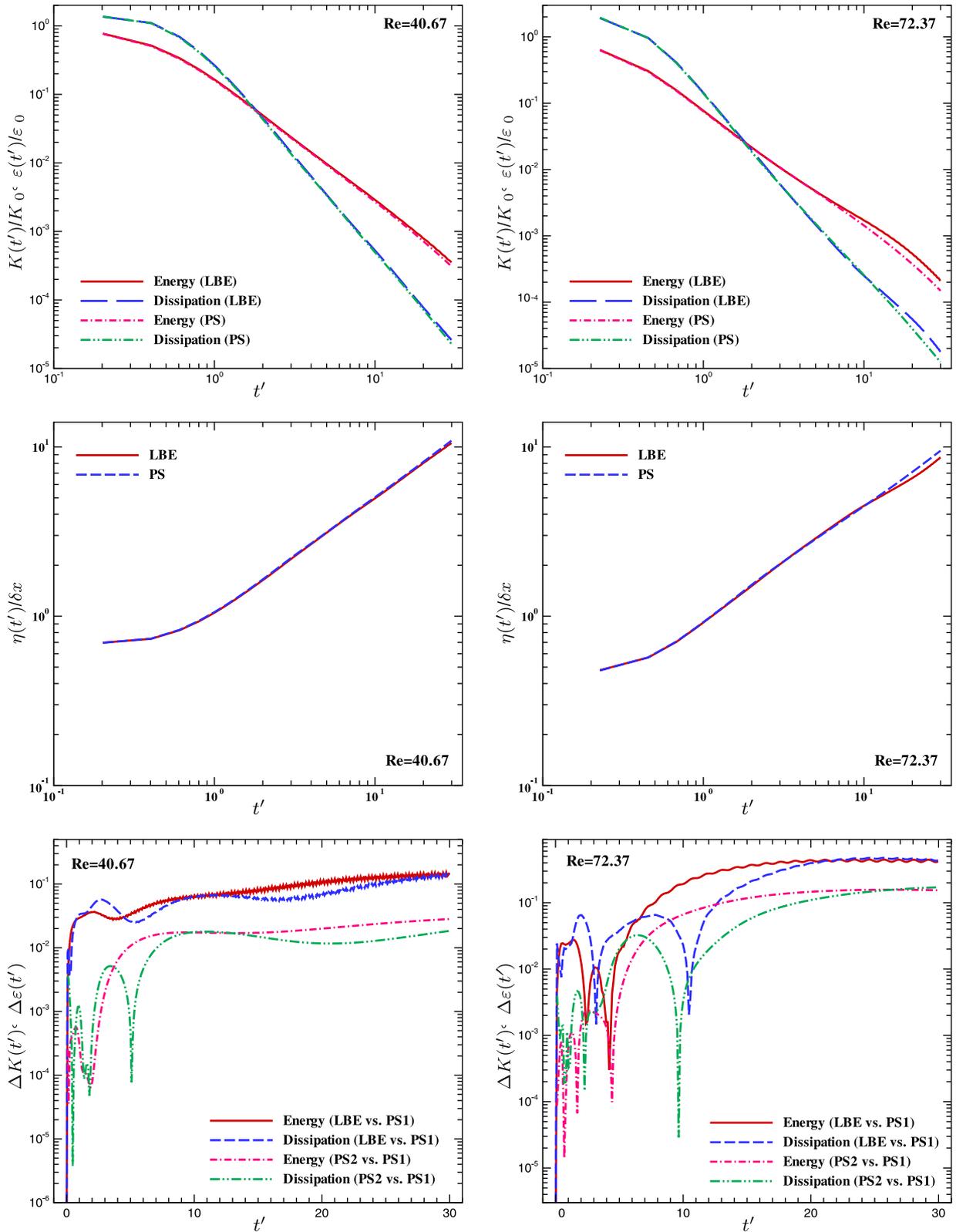
Fig. 21. Evolution of the normalized total kinetic energy $K(t')/K_0$ and the normalized dissipation rate $\varepsilon(t')/\varepsilon_0$ (top), the normalized Kolmogorov length $\eta(t')/\delta x$ (center), and the relative differences $\Delta K(t')$ and $\Delta \varepsilon(t')$ (bottom), with $N^3 = 128^3$, $Re_\lambda \approx 40.67$ (left) and 72.37 (right).

less computation than the PS method. As the number of CPUs increases while the system size N^3 maintains fixed, CPUs are increasingly under fed thus the data communication latency becomes a dominant factor accordingly. As for the memory use, the PS method requires 13 arrays of the size N^3, while the D3Q19 LBE model requires 19 arrays.

It should be pointed out that the initialization process in the LBE simulations is rather time consuming. In the present work, the

initialization takes almost as long as the simulation time, *i.e.*, about $30\tau_0$, where τ_0 is the turbulence turnover time, to satisfy the following criterion:

$$\max_{\boldsymbol{x}_j} \|\delta\rho(\boldsymbol{x}_j, t_n + 1) - \delta\rho(\boldsymbol{x}_j, t_n)\| \leqslant 10^{-8}.$$

To significantly shorten the time required to obtain accurate initial conditions in LBE simulations, either multigrid [46–48] or some implicit time integration [49] techniques must be used.

5. Discussion and conclusions

In this work we carry out a detailed comparison of the lattice Boltzmann and the pseudo-spectral methods for direct numerical simulations of decaying turbulence in three dimensions. We compare instantaneous flow fields and low-order statistical quantities computed by using these two methods. The computed instantaneous flow fields are the velocity field $\boldsymbol{u}(\boldsymbol{x}, t)$ and the vorticity field $\omega(\boldsymbol{x}, t)$. It is interesting to note that, while there have been numerous studies comparing turbulence statistics obtained by using finite-difference and spectral methods, to the best of knowledge, no detailed comparison of instantaneous flow fields has been made. Our results show that, with the Reynolds number Re_λ fixed, the L_2-normed difference $\|\delta\boldsymbol{u}\| := \|\boldsymbol{u}_{\mathrm{LBE}} - \boldsymbol{u}_{\mathrm{PS}}\|$ between the LBE and

PS velocity fields appear to grow linearly in time. Furthermore, the growth rate $d\|\delta\boldsymbol{u}\|/dt$ seems to depend linearly on Re_λ in a certain range Re_λ depending on the methods which are compared. As the Reynolds number Re_λ increases beyond certain point, the growth rate $d\|\delta\boldsymbol{u}\|/dt$ will saturate eventually. The same is also observed for the velocity difference between the velocity fields obtained by the PS method with different time step sizes. As for the vorticity field $\omega(\boldsymbol{x}, t)$, the L_2-normed difference $\|\delta\omega\| := \|\omega_{\mathrm{LBE}} - \omega_{\mathrm{PS}}\|$ between the LBE and PS vorticity fields exhibits a behavior entirely different from that of the velocity difference $\|\delta\mathrm{u}\|$. The vorticity difference $\|\delta\omega\|$ grows very rapidly in an initial period of time $t' < 2.0$, then increases gradually to a plateau in a later time. It is interesting to note that the same phenomenon is also observed in the vorticity difference between the vorticity fields obtained by the PS method with different time step sizes.

For the low-order statistical quantities, our results show that the energy spectrum $E(k, t)$, the total kinetic energy $K(t)$, and the dissipation rate $\varepsilon(t)$ obtained by the two methods agree very well up to $t' \approx 30$ when the initial velocity field is well resolved by both methods, *i.e.*, $\delta x/\eta_0 \leqslant 1.0$. This resolution criterion is consistent with previous empirical observations (cf. [42,43]). For the case of initial $\mathrm{Re}_\lambda = 24.35$, the relative differences in both $K(t)$ and $\varepsilon(t)$ computed by the LBE and PS methods are no more than 5% when $t' \approx 30$, after both $K(t)$ and $\varepsilon(t)$ decay almost four
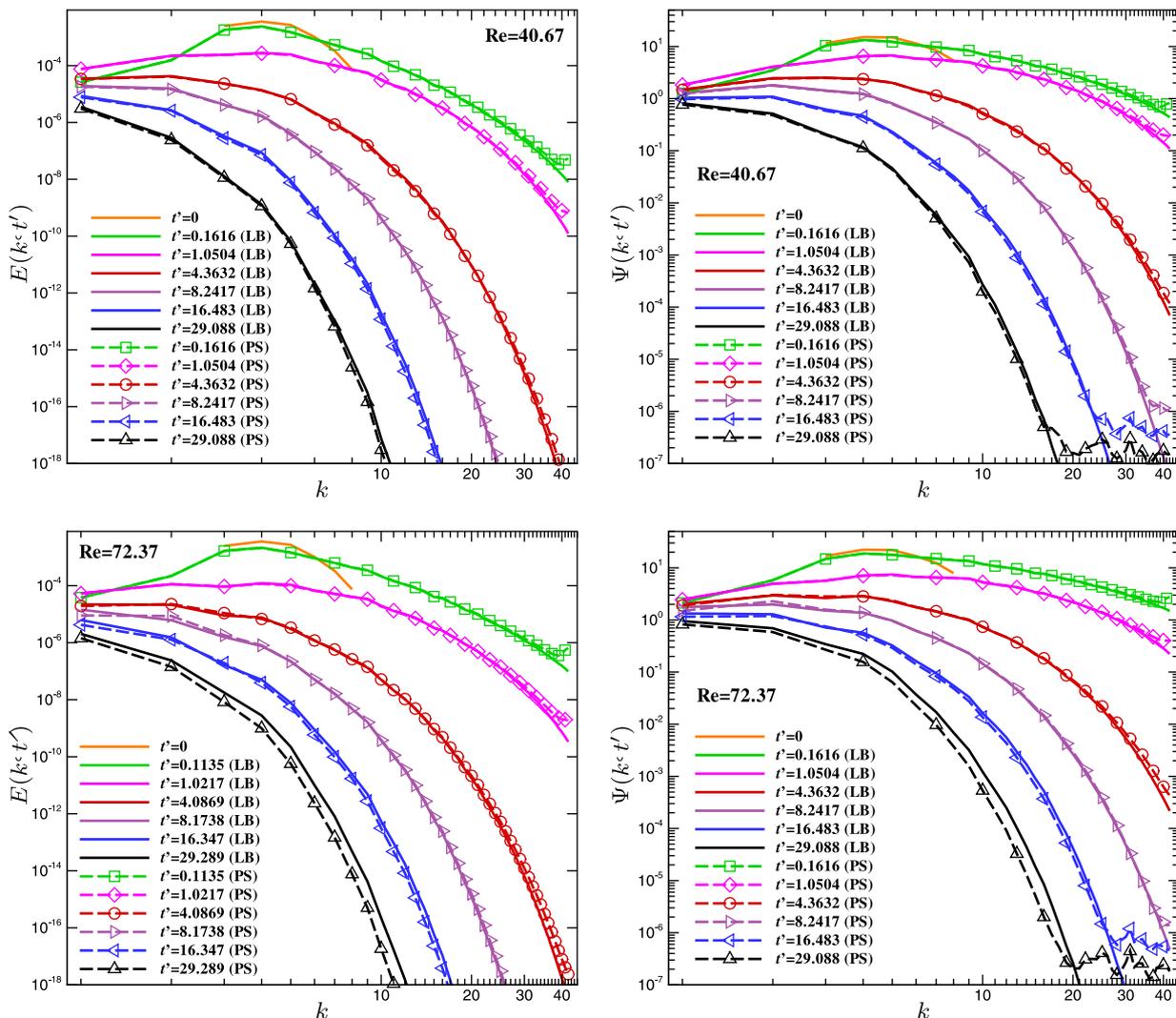

Fig. 22. The energy spectra $E(k, t)$ (left) and the compensated spectra $\Psi(k, t')$ (right) with $N^3 = 128^3$, $\mathrm{Re}_\lambda \approx 40.67$ (top) and 72.37 (bottom). The LBE (thin lines with symbols) vs. PS1 (thick patterned lines).
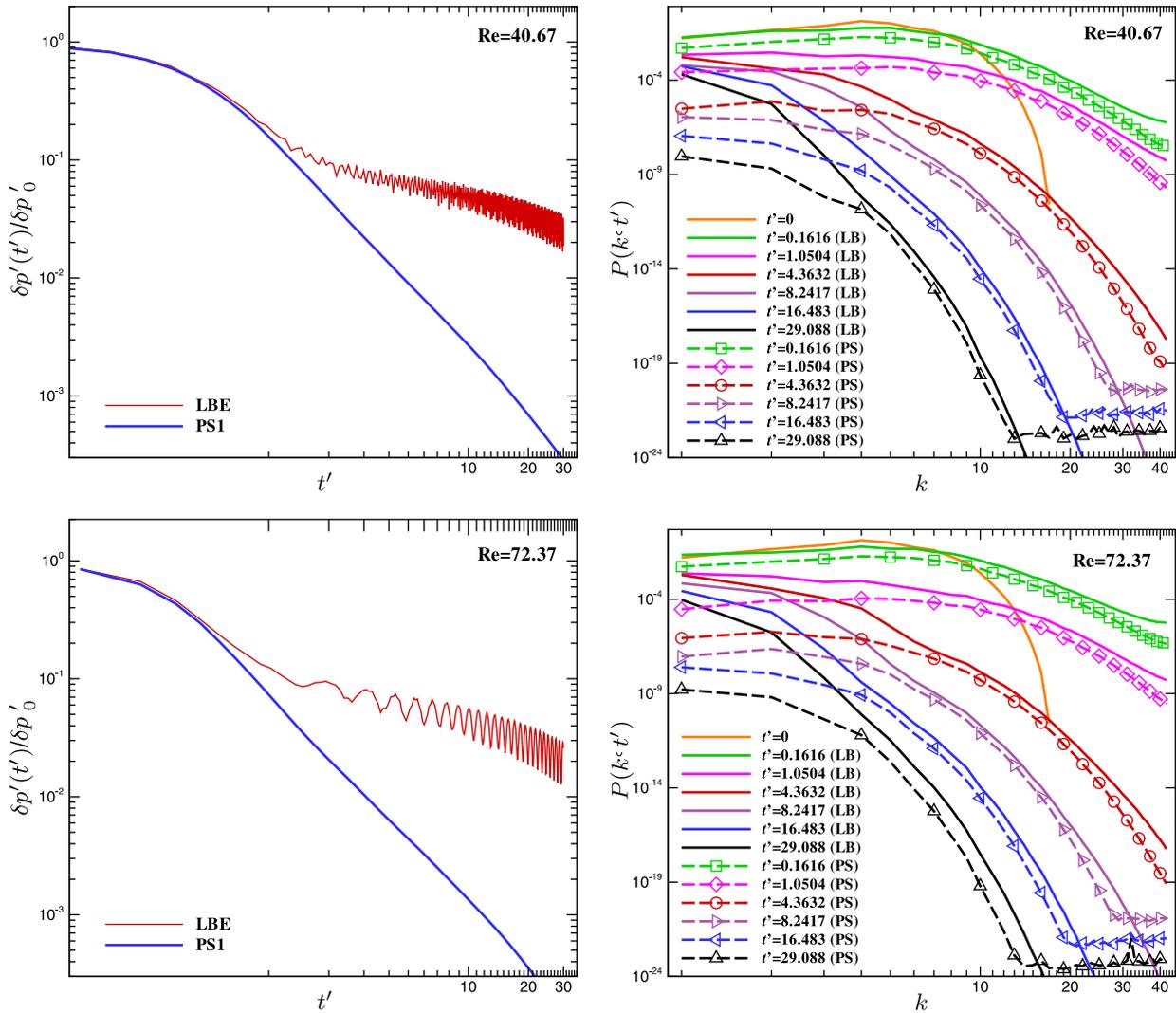
Fig. 23. The rms pressure fluctuation $\delta p'(t')/\delta p'_0$ (left) and the pressure spectra $P(k, t')$ (right), with Re ≈ 40.67 (top) and 70.37 (bottom). LBE vs. PS1.

orders of magnitude. This is not surprising, because the flow fields are well captured in the LBE calculation in this case. However, when the initial flow is under-resolved in the LBE simulations, such as in the case of initial Re$_\lambda \approx 72.37$ and $\eta_0/\delta x \approx 0.598$, $K(t)$ and $\varepsilon(t)$ computed from the two methods show visible discrepancies after $t' > 10$, and the relative differences in $K(t)$ and $\varepsilon(t)$ computed by the LBE and PS methods increase to about 40% when $t' > 20$. However, even in the case of Re$_\lambda = 72.37$, both $K(t)$ and $\varepsilon(t)$ computed from the two methods agree well when $t' \approx 10$. In general, the relative differences $\Delta K(t)$ and $\Delta\varepsilon(t)$ for the LBE vs. PS method are greater than their counterparts for the PS method with different $\delta t'$. However, the differences between $\Delta K(t)$ and $\Delta\varepsilon(t)$ for the LBE vs. PS method, and their counterparts for the PS method with different $\delta t'$, decrease as the Reynolds number Re$_\lambda$ increases.

The greatest difference between statistical quantities computed by using the LBE and PS methods is the pressure spectrum $P(k, t')$, due to significantly different treatments of the pressure field $p(\boldsymbol{x}, t)$ in these two methods. It can be shown that the spatial accuracy of the pressure field p solved by the LBE method is formally first-order. As shown in the present work, even when the flow is well resolved initially by both methods, *i.e.*, $\delta x/\eta_0 \leqslant 1.0$, the rms pressure fluctuations obtained by the LBE and PS methods agree with each other very well only for a relatively short period of time $t' < 2.0$.

Consequently the pressure spectra $P(k, t')$ computed by using the two methods also agree with each other in the same short period of time. Increasing the grid Reynolds number Re$_\lambda/N$ would decrease this initial period of time within which the pressures computed by using the two methods agree with each other. Beyond this initial period of time, the quality of the LBE pressure field deteriorates and is dominated by density fluctuations of very high frequencies and short wavelengths, comparable to that of the time step size δt and the grid spacing δx, respectively. In spite of the deterioration of the pressure field, both velocity and vorticity fields are well captured in the LBE simulations.

For the skewness and flatness of the velocity derivative, the effect due to acoustic waves intrinsic to the LBE method is conspicuous: the pressure fluctuations induce high-frequency oscillations in the skewness and the flatness computed by using the LBE method, which are absent in the PS results. Nevertheless, when the high-frequency oscillations are filtered out, the LBE results agree well with the PS results up to $t \approx 30\tau_0$ when the initial flow field is well resolved by both methods, as in the case of Re$_\lambda \approx 24.35$.

Based on our results, we can conclude that, overall, the lattice Boltzmann method performs very well when compared with the pseudo-spectral method for DNS of decaying turbulence when the flow is properly resolved. Specifically, the LBE simulations can reliably produce accurate results for instantaneous velocity
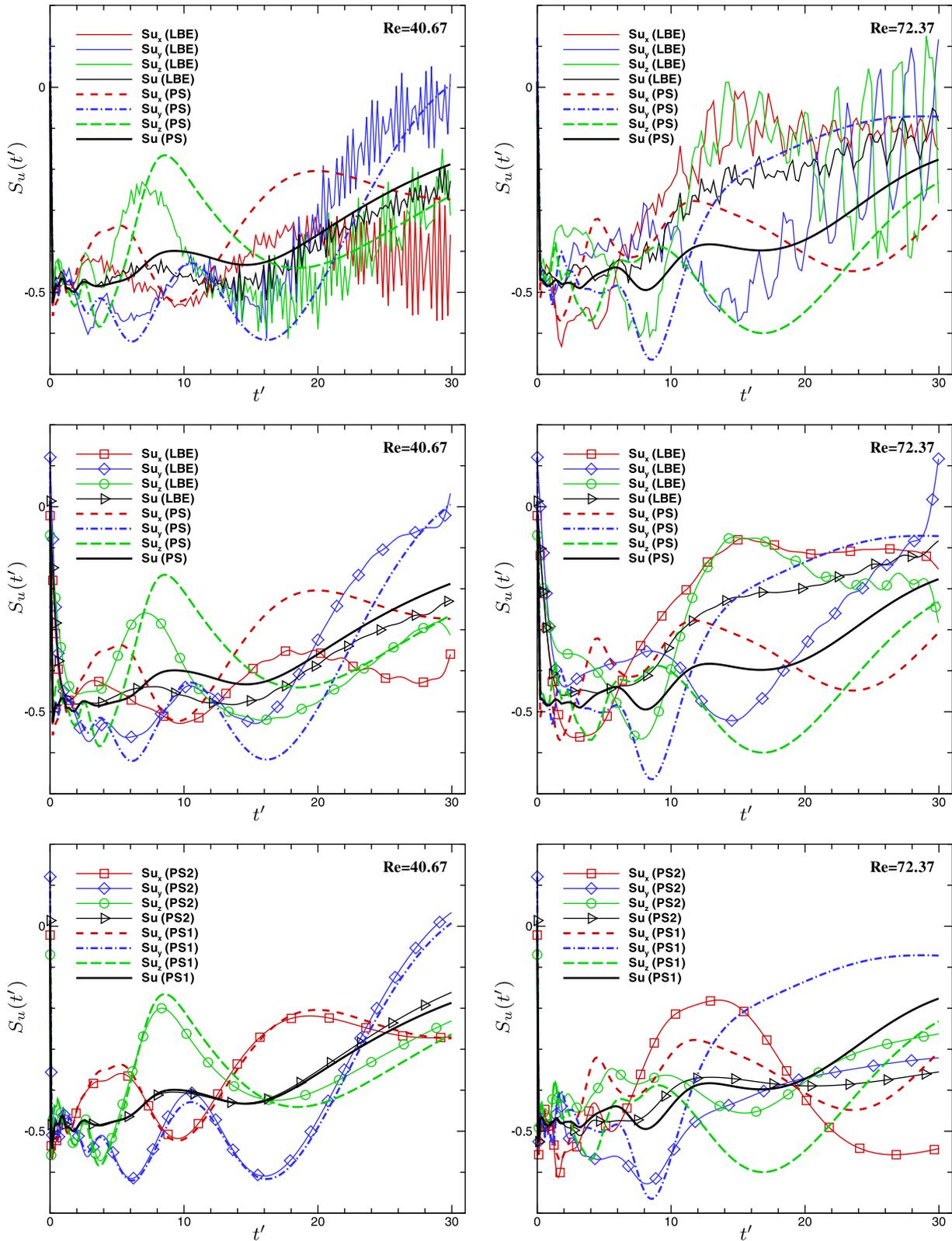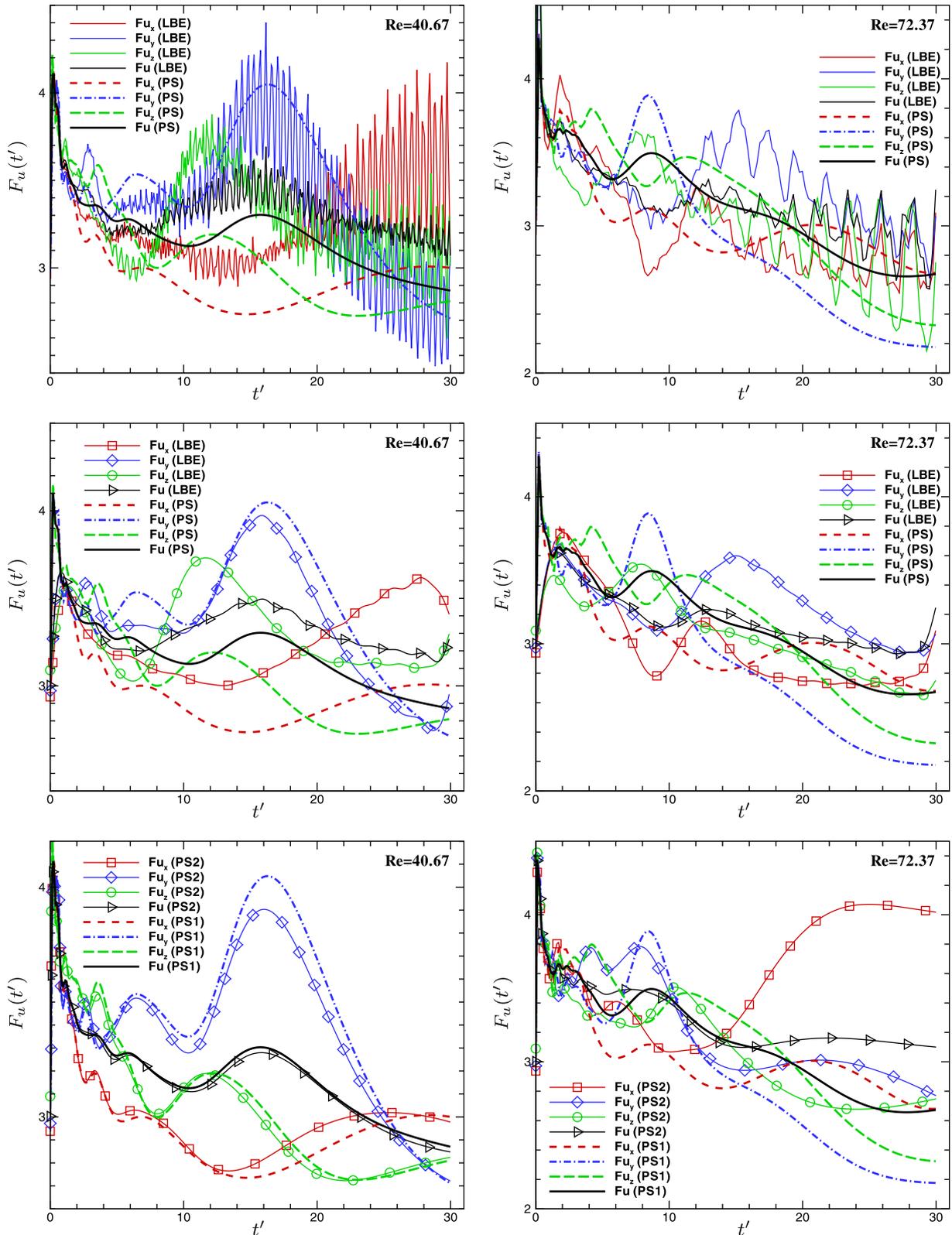
Fig. 24. The skewness with Re$_\lambda \approx 40.67$ (left) 72.37 (right). $N^3 = 128^3$. LBE vs. PS1 (top), smoothed LBE vs. PS1 (center), and PS2 vs. PS1 (bottom).

and vorticity fields and low-order statistical quantities including the total energy $K(t)$, the dissipation rate $\varepsilon(t)$, the energy spectrum $E(k, t)$, the skewness and the flatness for an extended period of time, provided that the initial flow field is well resolved with the criterion that $\delta x/\eta_0 \leqslant 1.0$, which is about twice of the resolution

requirement for spectral methods. This is consistent with the observation made in a previous study comparing finite-difference and spectral methods [42,43,31]. Consequently the LBE method demands a computational effort about 16 times greater than that of the pseudo-spectral method (a factor of two from each spatial

Fig. 25. The flatness with Re$_\lambda \approx 40.67$ (left) 72.37 (right). $N^3 = 128^3$. LBE vs. PS1 (top), smoothed LBE vs. PS1 (center), and PS2 vs. PS1 (bottom).

dimension and another one from time stepping, to maintain the same CFL number in both systems). However, this is expected because the LBE method is only a second-order scheme. The pressure field obtained by using the LBE method is much less satisfactory. The rms pressure $\delta p'(t)$ and the pressure spectrum $P(k, t)$ obtained

by using the LBE method are accurate in a time interval much shorter than that for the velocity field and other statistical quantities. This is somewhat expected because the LBE method does not solve the Poisson equation for the pressure, and this is true of all low-order schemes which do not solve the Poisson equation
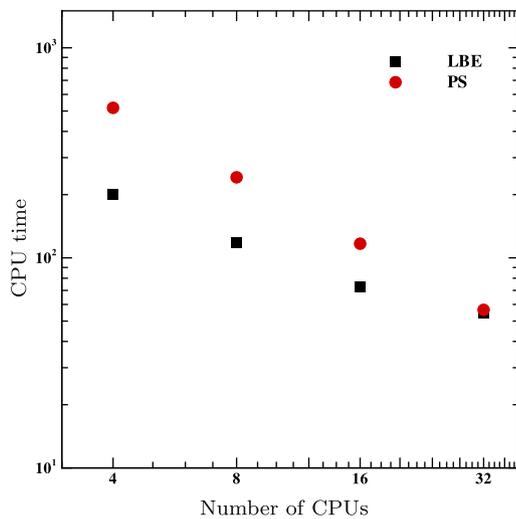
Fig. 26. Parallel efficiency, LBE (squares) vs. PS (bullets) method.

accurately. To improve the accuracy of the LBE method for the pressure field, one must, in some way, consider solving the Poisson equation effectively and efficiently while preserving other key features of the LBE method, including its conservativeness, isotropy, and low numerical dissipation in small scales [33,36]. This will be a subject of our future research.

Finally, we would like to comment on the significance of this work. In a larger sense, our work attempts to address the following question: what should we understand by "direct numerical simulations" for turbulence? For many, DNS may simply mean a numerical method without explicit turbulence modeling. However, it is more appropriate to restrict the term "DNS" to schemes which demonstrably resolve everything up to the smallest dynamically relevant scale. In this sense, spectral-type methods are the best methods to perform "DNS", and we have shown in this work that, although the LBE method is inferior to pseudo-spectral methods in terms of accuracy, it can nevertheless be used as an adequate "DNS" tool. We believe that the success of the LBE method as a DNS tool can be specifically attributed to the following features of the LBE. First, the LBE method has relatively low numerical dissipations even at the scales of grid spacing [33,36], which is difficult to achieve for low-order schemes. Second, the LBE method is isotropic, that is, its accuracy does not depend on the angle with respect to mesh lines [33,36]. The isotropy ensures the conservation of angular momentum (or vorticity) numerically. And third, the LBE method has relatively small numerical dispersive effects [33], which are certainly less than what is observed in conventional CFD methods of second-order accuracy [50,51]. These insights can serve as guidelines to construct accurate numerical schemes for DNS of turbulence.

Acknowledgments

References

[1] Pope SB. Turbulent flows. Cambridge, UK: Cambridge University Press; 2000.
[2] Sagaut P, Cambon C. Homogeneous turbulence dynamics. New York: Cambridge University Press; 2008.
[3] Orszag SA, Patterson GS. Numerical simulation of three-dimensional homogeneous isotropic turbulence. Phys Rev Lett 1972;28(2):76–9.
[4] Canuto CG, Hussaini MY, Quarteroni A, Zang TA. Spectral methods: evolution to complex geometries and applications to fluid dynamics. New York: Springer; 2007.
[5] Vincent A, Meneguzzi M. The spatial structure and statistical properties of homogeneous turbulence. J Fluid Mech 1991;225:1–20.
[6] Jiménez J, Wray A, Saffman PG, Rogallo R. The structure of intense vorticity in isotropic turbulence. J Fluid Mech 1993;255:65–90.
[7] Wang L-P, Chen S-Y, Brasseur JG, Wyngaard JC. Examination of hypotheses in the Kolmogorov refined turbulence theory through high-resolution simulations 1. Velocity field. J Fluid Mech 1996;309:113–56.
[8] Jiménez J, Wray A. On the characteristics of vortex filaments in isotropic turbulence. J Fluid Mech 1998;273:255–85.
[9] Gotoh T, Fukayama D. Pressure spectrum in homogeneous turbulence. Phys Rev Lett 2001;86(17):3775–8.
[10] Kaneda Y, Ishihara T, Yokokawa M, Itakura K, Uno A. Energy dissipation rate and energy spectrum in high resolution direct numerical simulations of turbulence in a periodic box. Phys Fluids 2003;15(2):L21–4.
[11] Yoshida K, Yamaguchi J, Kaneda Y. Regeneration of small eddies by data assimilation in turbulence. Phys Rev Lett 2005;94(1):014501.
[12] Ishida T, Davidson PA, Kaneda Y. On the decay of isotropic turbulence. J Fluid Mech 2006;564:455–75.
[13] Kaneda Y, Ishihara T. High-resolution direct numerical simulation of turbulence. J Turbul 2006;7(20):1–17.
[14] Donzis DA, Yeung PK, Sreenivasan KR. Dissipation and enstrophy in isotropic turbulence: resolution effects and scaling in direct numerical simulations. Phys Fluids 2008;20(4):045108.
[15] Ishihara T, Gotoh T, Kaneda Y. Study of high-Reynolds number isotropic turbulence by direct numerical simulations. Annu Rev Fluid Mech 2009;41:165–80.
[16] He X, Luo L-S. A priori derivation of the lattice Boltzmann equation. Phys Rev E 1997;55(6):R6333–6.
[17] He X, Luo L-S. Theory of lattice Boltzmann method: from the Boltzmann equation to the lattice Boltzmann equation. Phys. Rev. E 1997;56(6):6811–7.
[18] Yu DZ, Mei R, Luo L-S, Shyy W. Viscous flow computations with the method of lattice Boltzmann equation. Prog Aerospace Sci 2003;39(5):329–67.
[19] Chen S, Wang Z, Shan X, Doolen GD. Lattice Boltzmann computational fluid dynamics in three dimensions. J Stat Phys 1992;68(3/4):379–400.
[20] Treviño C, Higuera F. Lattice Boltzmann and spectral simulations of nonlinear stability of Kolmogorov flows. Revista Mexicana de Fisica 1994;40(6):878–90.
[21] Luo L-S, Qi D, Wang L-P. Applications of the lattice Boltzmann method to complex and turbulent flows. In: Breuer M, Durst F, Zenger C, editors. High performance scientific and engineering computing. Lecture notes in computational science and engineering, vol. 21. Berlin: Springer; 2002. p. 123–30.
[22] Yu HD, Girimaji SS, Luo L-S. Lattice Boltzmann simulations of decaying homogeneous isotropic turbulence. Phys Rev E 2005;71(1):016708.
[23] Yu HD, Girimaji SS, Luo L-S. DNS and LES of decaying isotropic turbulence with and without frame rotation using lattice Boltzmann method. J Comput Phys 2005;209(2).
[24] Yu DZ, Girimaji SS. Direct numerical simulations of homogeneous turbulence subject to periodic shear. Phys Rev E 2005;71(1):016708.
[25] Yu DZ, Girimaji SS. DNS of homogeneous shear turbulence revisited with the lattice Boltzmann method. J Turbul 2005;6(6).
[26] Hazi G. Bias in the direct numerical simulation of isotropic turbulence using the lattice Boltzmann method. Phys Rev E 2005;71(3):036705.
[27] Izawa WA Kareem S, Xiong AK, Fukunishi Y. Identification of multi-scale coherent eddy structures in a homogeneous isotropic turbulence. Prog Comput Fluid Dyn 2006;6(7):402–8.
[28] ten Cate A, van Vliet E, Derksen JJ, Van den Akker HEA. Application of spectral forcing in lattice-Boltzmann simulations of homogeneous turbulence. Comput. Fluids 2006;35(10):1239–51.
[29] Burattini P, Lavoie P, Agrawal A, Djenidi L, Antonia RA. Power law of decaying homogeneous isotropic turbulence at low Reynolds number. Phys. Rev. E 2006;73(6):066304.
[30] Orlandi P. Fluid flow phenomena. Dordrecht: Kluwer; 2000.
[31] Yoshimatsu K, Ishihara T, Kaneda Y, Nakai S, Nishida H, Satofuka N. Comparison of a spectral method with a higher-order finite difference method in direct numerical simulations of three-dimensional homogeneous turbulence. Trans Jpn Soc Mech Eng Ser B 2003;69(679):13–8 [in Japanese].
[32] d'Humières D. Generalized lattice-Boltzmann equations. In: Shizgal BD, Weave DP, editors. Rarefied gas dynamics: theory and simulations. Progress in astronautics and aeronautics, vol. 159. Washington, DC: AIAA; 1992. p. 450–8.
[33] Lallemand P, Luo L-S. Theory of the lattice Boltzmann method: dispersion, dissipation, isotropy, Galilean invariance, and stability. Phys Rev E 2000;61(6):6546–62.

[34] d'Humières D, Bouzidi M, Lallemand P. Thirteen-velocity three-dimensional lattice Boltzmann model. Phys Rev E 2001;63:066702.

[35] d'Humières D, Ginzburg I, Krafczyk M, Lallemand P, Luo L-S. Multiple-relaxation-time lattice Boltzmann models in three-dimensions. Philos Trans Roy Soc Lond A 2002;360(1792):437–51.

[36] Lallemand P, Luo L-S. Theory of the lattice Boltzmann method: acoustic and thermal properties in two and three dimensions. Phys Rev E 2003;68(3):036706.

[37] He X, Luo L-S. Lattice Boltzmann model for the incompressible Navier–Stokes equation. J Stat Phys 1997;88:927–44.

[38] Rogallo RS. Numerical experiments in homogeneous turbulence. Technical Report TM-8135, NASA; 1981.

[39] Yeung PK, Pope SB. Lagrangian statistics from direct numerical simulations of isotropic turbulence. J Fluid Mech 1989;207:531–86.

[40] Junk M, Klar A. Discretizations for the incompressible Navier–Stokes equations based on the lattice Boltzmann method. SIAM J Sci Comput 2000;22:1–19.

[41] Junk M, Klar A, Luo L-S. Asymptotic analysis of the lattice Boltzmann equation. J Comput Phys 2005;210(2):676–704.

[42] Kristoffersen R, Andersson HI. Direct simulations of low-Reynolds-number turbulent flow in a rotating channel. J Fluid Mech 1993;256:163–97.

[43] Moin P, Mahesh K. Direct numerical simulation: a tool in turbulence research. Annu Rev Fluid Mech 1998;30:539–78.

[44] Mei R, Luo L-S, Lallemand P, d'Humières D. Consistent initial conditions for lattice Boltzmann simulations. Comput Fluids 2006;35:855–62.

[45] Clark TT, Zemach C. Symmetries and the approach to statistical equilibrium in isotropic turbulence. Phys Fluids 1998;10(11):2846–58.

[46] Tölke J, Krafczyk M, Rank E. A multigrid solver for the discrete Boltzmann equation. J Stat Phys 2002;107:573–91.

[47] Mavriplis DJ. Multigrid solution of the steady-state lattice Boltzmann equation. Comput Fluids 2005;35(8/9):793–804.

[48] Mavriplis DJ. Exploring alternative approaches to computational fluid dynamics. Int J Comput Fluid Dyn 2005;19(8):613–20.

[49] Tölke J, Krafczyk M, Schulz M, Rank E, Berrios R. Implicit discretization and nonuniform mesh refinement approaches for FD discretizations of LBGK models. Int J Mod Phys C 1998;9:1143–57.

[50] Wilde A. Calculation of sound generation and radiation from instationary flows. Comput Fluids 2006;35(8/9):986–93.

[51] Maríe S, Ricot D, Sagaut P. Comparison between lattice Boltzmann method and Navier–Stokes high-order schemes for computational aeroacoustics. J Comput Phys 2009;228(4):1056–70.